2016-05-01

Error Propagation Dynamics of PIV-based Pressure Field Calculation

Zhao Pan
Brigham Young University

Error Propagation Dynamics of PIV-based Pressure Field Calculation

Zhao Pan

A dissertation submitted to the faculty of
Brigham Young University
in partial fulfillment of the requirements for the degree of

Doctor of Philosophy

Tadd T. Truscott, Chair
Jared P. Whitehead
John C. Dallon
Julie Crockett
Daniel R. Maynes

Department of Mechanical Engineering

Brigham Young University

May 2016

ABSTRACT

Error Propagation Dynamics of PIV-based Pressure Field Calculation

Zhao Pan
Department of Mechanical Engineering, BYU
Doctor of Philosophy

Particle Image Velocimetry (PIV) based pressure field calculation is becoming increasingly popular in experimental fluid dynamics due to its non-intrusive nature. Errors propagated from PIV results to pressure field calculations are unavoidable, and in most cases, non-negligible. However, the specific dynamics of this error propagation process have not been unveiled. This dissertation examines both why and how errors in the experimental data are propagated to the pressure field by direct analysis of the pressure Poisson equation. Error in the pressure calculations are bounded with the error level of the experimental data. The error bounds quantitatively explain why and how many factors (i.e., geometry and length scale of the flow domain, type of boundary conditions) determine the resulting error propagation. The reason that the type of flow and profile of the error matter to the error propagation is also qualitatively illustrated. Numerical and experimental validations are conducted to verify these results. The results and framework introduced in this research can be used to guide the optimization of the experimental design, and potentially estimate the error in the reconstructed pressure field before performing PIV experiments.

Keywords: PIV, pressure calculation, error propagation, error bound

ACKNOWLEDGMENTS

Sincere thanks to Dr. Tadd Truscott for years support, especially the freedom he gave me to exploring around. I tried many different projects in the Splash lab in the last three years, from PIV algorithms, surface phenomena, aerodynamics of sports to water impact problems, etc., but most of them either already failed, or are under very slow progress. However, his trust and guidance gives me confidence and flexibility to doodle around and work slowly under my own rhythm, and lead to this dissertation study fulfilled.

Acknowledgment to my committee members for constructive suggestions and guidance. Thanks to Dr. Xiaofeng Liu and Dr. Ronland de Kat for suggestions to Chapter 4. Thanks to Dr. John Charonko and Dr. Barton Smith for providing experimental data used in Chapter 5. Many thanks to Dr. Scott Thomson for introducing the PIV-based pressure calculation problem to me at very early stage of my Ph.D studies, which is a problem that is tractable enough for a student yet rich enough to be attractive to both engineering and applied mathematics community.

Special thanks to Dr. Jared Whitehead who guided me to break through whenever I am stuck by mathematics and corrected so many of my careless/skilless derivations. I wish BYU hired him earlier. I am always amazed by his open mind as well as precise intuition to physics and math, which lead to break-through after very few even only one attempt. Without his help I cannot even see my dissertation could be on this topic.

Special thanks to Dr. William Pitt for his teaching and mentorship in past few years regarding to the surface phenomenon, although this topic is not covered in this dissertation.

Thanks for Mr. Randy Hurd for taking care of me in many ways here. He made my life, in and outside school, in this foreign land much less stressed and more colorful.

Dedicate to my dear wife, Dr. Wenyan Jiang, and the slogan of our family carved on our wedding rings "*Stupid* ∞" [1] and "*Fool* ∞" [2].

[1] Mine.
[2] Hers.

TABLE OF CONTENTS

LIST OF TABLES

LIST OF FIGURES

A	Area of the domain
C_D	Poincare constant of a domain with Dirichlet boundary conditions
C_N	Poincare constant of a domain with Neumann boundary conditions
C_{NB}	Poincare constant of a Neumann boundary
J_0	Bessel function of the first kind of zero order
J_1	Bessel function of the first kind of first order
K	Layer-specific stiffness constant
L_0	Characteristic length scale of a flow
L	Length scale of a domain
M	Width of a rectangular domain
N	Height of a rectangular domain
P_0	Characteristic pressure of a flow
R_{fb}	Contribution ratio of the field to the boundary
U_0	Characteristic velocity of a flow
$\boldsymbol{u}$	Velocity field
$\tilde{p}$	Error contaminated pressure field
p	Pressure field
u	Velocity component in x direction
v	Velocity component in y direction
Ω	Flow domain
$\partial\Omega$	Boundary of a flow domain
α	Aspect ratio of a rectangular domain
ϵ	Error field
ζ	Mass-proportional damping coefficient
η	Stiffness-proportional damping coefficient
μ	Dynamic viscosity
ν	Kinematic viscosity
ρ	Density of fluid
σ	Stress
ξ	Strain

Subscripts, superscripts, and other indicators

$[\,]^*$	Indicates $[\,]$ is a non-dimensionalized variable
$\bar{[\,]}$	Indicates $[\,]$ is an averaged value
$\hat{[\,]}$	Indicates $[\,]$ is an estimated value
$\tilde{[\,]}$	Indicates $[\,]$ is an error contaminated variable
$[\,]_0$	Indicates $[\,]$ is a characteristic variable
$[\,]_f$	Indicates $[\,]$ refers to the field
$[\,]_g$	Indicates $[\,]$ refers to the Neumann boundary
$[\,]_h$	Indicates $[\,]$ refers to the Dirichlet boundary
$[\,]_{(\mathscr{L})}$	Indicates $[\,]$ refers to a Laplace problem
$[\,]_{(\mathscr{P})}$	Indicates $[\,]$ refers to a Poisson problem

CHAPTER 1. INTRODUCTION

1.1 Overview

Pressure and velocity measurements are essential to the experimental investigation of fluid dynamics. Perhaps the most capable method for measuring the velocity field of a fluid flow is particle image velocimetry (PIV). The non-intrusive nature of PIV is fundamental to its popularity. As PIV quality increases, PIV-based pressure calculations (using either Naiver-Stokes or the pressure Poisson equation) are under growing investigation to establish a non-invasive pressure field measurement technique. However, the error inherent in PIV measurement is unavoidable and these experimental errors will inevitably propagate from the velocity field measurements to pressure field calculations, leading to potentially unreliable pressure calculations.

In this dissertation, I discuss the error propagation dynamics of PIV-based pressure calculation, how velocity field error propagates to the pressure field through the pressure Poisson equation, and the factors that affect this error propagation dynamics including: boundary conditions, domain shape and scale, etc. Additionally, I provide suggestions regarding the optimization of experimental PIV settings to minimize propagated error.

1.2 Summary

This dissertation focuses on particle image velocimetry (PIV) based pressure calculations, with particular emphasis on the error propagation from the velocity field to the pressure field through the calculation scheme. This dissertation will be organized chronologically as a summary of the Ph.D studies of the author.

PIV-based pressure calculations are popular techniques for non-intrusive pressure measurements [1]. Literature related to PIV-based pressure calculation techniques are briefly reviewed in Chapter 2 to provide background for this work. Studies on calculating pressure fields from ve-

locity field data date back to Schwabe's work in 1935 [2], and is drawing increasing attention recently [1], in spite of its unreliable tendencies (e.g. sensitive to boundary conditions, flow type and calculation schemes) [3].

In Chapter 3, a calculation scheme based on a Poisson solver is developed. The first order finite difference method is used to create a Poisson solver capable of solving Poisson equations in the 2D Cartesian domain with either Neumann or Dirichlet boundary conditions. By taking advantage of the scalar property of the pressure field, a multipath strategy, similar to the method proposed by Dabiri et al. [4] is implemented and applied to a laminar glottal flow (flow between synthetic vocal folds). Error analysis in terms of spatial and temporal resolutions is conducted by comparing the results to a two dimensional computational fluid dynamics (CFD) simulation. This initial study inspires the remainder of this dissertation.

Chapter 4 reports the error propagation dynamics of the PIV-based pressure field calculation. I clearly specify the error-contaminated Poisson problem raised by the pressure field calculation from noisy PIV experiments. This engineering problem is then translated into an applied mathematical problem, specifically by obtaining bounds on solutions of a Poisson equation. Rigorous bounds on the error in the pressure calculation, relative to the error inherent from the PIV measurements, are also presented. Several typical examples are shown, and I discuss the limitations and practical uses of this work.

In Chapter 5 I present an example that illustrates how to use the results in Chapter 4 to design and optimize experiments. For the sake of simplicity, a Taylor-Green vortex field is used as a synthetic flow to discuss how factors such as: boundary conditions, length scale of the flow field, nondimensionalization, etc., affect the error propagation from the velocity field to the pressure field. This section also serves as a more detailed numerical validation to the results in Chapter 4.

Chapter 6 summarizes an experimental validation based on a two dimensional oscillating flow in a diffuser (data from PIV and pressure ports can be found in works by King and Smith [5]). Due to data limitations, I only test how the aspect ratio and length scale of the domain affect the error propagation for cases with Neumann boundary conditions.

Chapter 7 lists two open problems raised by this dissertation to be considered for future studies.

CHAPTER 2. BACKGROUND

In this section, I briefly review the studies of the PIV-based pressure calculations to provide background for my research regarding the error propagation dynamics of PIV-based pressure calculations, which has not been widely studied.

Accurate pressure and velocity measurements are critical for experimental fluid dynamics. Historically, flow velocity has been measured using various techniques including hot wire anemometry [6] and laser doppler velocimetry [7, 8]. More recently, digital imaging techniques such as Particle Image Velocimetry (PIV) [9] and Particle Tracking Velocimetry (PTV) [10] have proven to be effective techniques that are continually improving. Perhaps the most attractive feature of PIV techniques is their noninvasive nature. In contrast, pressure measurements are still primarily based on the probe or port methods [11, 12]. These point-wise measurements typically disturb the flow and only provide pressure information at a limited number of specific points.

One category of field measurement techniques for pressure acquisition employs pressure sensitive particles or materials. For example, Ran and Katz [13] were able to measure pressure distribution within water jets using microscopic air bubbles as pressure sensors because the size of the bubble changes with ambient pressure. Recently, pressure sensitive paint (PSP) has been widely applied in flow diagnostic techniques [14]. When exposed to laser light, a surface covered with PSP emits illumination with different intensity under pressure differences. For example, Fujii et al. [15] fabricated Anodized-Aluminum PSP and captured the pressure distribution around a cylinder as it was traversed by a shock wave. The frequency response of the PSP they used is fast enough to clearly catch both the Mach stem and the triple point. PSP can also be used to generate micro-particles to be used as PIV tracers. Kimura et al. [16] employed pressure sensitive micro-spheres in a PIV setting to measure the pressure and velocity distribution in an air-filled syringe chamber with the plunger moving in and out. This technique enabled simultaneous and non-intrusive collection of pressure and velocity field data. However, the pressure-sensitive micro

beads used in this technique actually measure oxygen content changes more readily than pressure changes making its application limited to experimental flows with relatively low values of dissolved oxygen. Moreover, the fabrication of PSP or pressure sensitive tracers, and the complex calibration required, make this application significantly more inconvenient than traditional PIV.

A more straightforward method for non-intrusive pressure field measurement is a natural extension of PIV. It involves a non-intrusive quantification of the pressure field using the Navier-Stokes equation and the velocity field from standard PIV measurements.

Early efforts at noninvasive pressure estimates can be traced back to Schwabe (1935) [2]. In his early work, tracer particles flowing around a cylinder were photographed with long exposure times. The lengths of the resulting streaklines were used to estimate the velocity field. The pressure field was calculated by integrating along the streamlines on gridded paper and utilizing the unsteady Bernoulli equation to estimate the corresponding values. This pioneering work was accomplished using calculations made by Prandtl nearly 80 years ago, when digital images and computers were not available (as mentioned by van Oudheusden [1]). In 1983, Imaichi and Ohmi [17] used a computer to process similar streakline images to obtain the velocity field for the flow around a cylinder. The velocity field was interpolated for computational analysis and a finite difference method was employed to integrate the Navier-Stokes equation to obtain the pressure distribution in the flow field. However, due to the technical limitations of their imaging technique (i.e., low spatial and temporal resolution, etc.) and consequently large error in the velocity field measurement, the pressure calculations were not accurate enough to ensure quantitative confidence.

After more than 20 years of development, PIV has become a standard non-invasive velocity field measurement technique [18]. Continual improvement has led to high temporal and spatial resolution for modern PIV techniques and even time resolved volumetric PIV [19, 20]. Several groups have revisited velocity field based pressure calculation techniques and applied them to many different areas. De Kat and Van Oudheusden reported their work on applying high-speed PIV to planar pressure calculations in a turbulent flow field. Stereoscopic and tomographic PIV systems were used to measure out-of-plane velocity components in a flow passing over a square extrusion (Re=9,500) [21]. For the turbulent case, they recommended that the interrogation window be 5 times smaller than the flow structures, and that the sampling frequency (acquisition frequency) of the PIV system be 10 times smaller than the flow frequency. Van Oudheusden et al. extended

the previous work to compressible flows [22, 23]. PIV data from an airfoil in a supersonic flow and shock wave boundary layer interactions were used to successfully estimate the corresponding pressure field.

Other examples include works by Lignarolo et al. [24] and Villegas and Diez [25] who used PIV data to calculate the pressure in a wind turbine. In water, PIV data was used to obtain the wall pressure of a wedge slamming into the water by both Panciroli and Porfiri [26] and Nila et al. [27], independently. The aero-acoustics community has also employed PIV-based pressure measurements; acoustic analogies are often utilized to estimate sound fields using PIV data [28–30].

Unfortunately, uncertainties in the PIV-based velocity field measurement will always propagate to contaminate the resulting pressure field calculation. Researchers have noticed this issue and several techniques have been developed to reduce the errors in the resulting pressure field. One popular strategy is to average several pressure calculations along different integral paths by taking advantage of the scalar property of the pressure field (the integrated pressure value at an arbitrary location in the flow field is independent of the integral path). Baur and Köngeter directly integrated a simplified Navier-Stokes equation with an explicit scheme [31]. They utilized time-resolved PIV data to determine the pressure of a turbulent flow passing over a wall. At each nodal point, four integrals were calculated from neighboring nodes and averaged to formulate the pressure estimation. However, they only commented on the accuracy of the PIV, not that of the pressure estimation.

A further reduction in the error accumulation from the uncertainties in PIV data was implemented by Liu and Katz [32]. They proposed an omni-directional integration scheme to directly integrate the pressure gradient from a virtual boundary outside the flow field. For an $M \times N$ mesh, the pressure value at each nodal point is integrated along $2(M+N)$ different paths, and the mean value of these $2(M+N)$ integrals is used as the estimation of the local pressure. This approach leads to significant cancelations if the error is truly random. This method was validated using a synthetic flow and then applied to a cavity flow. This approach is likely the most capable of removing the most significant portion of the random error. Dabiri et al. proposed an algorithm that used the median of the pressure calculated by integrating the pressure gradient along eight paths to estimate the local pressure at each point in the field [4]. To reduce the uncertainties in the velocity field from the PIV, a temporal filter was utilized to cancel the inherent noise, and this approach

was applied to the flow around free swimmers (e.g., jellyfish and lamprey). Taking advantages of the scalar property of the pressure field improves the accuracy of the pressure calculation, however, these studies provide little insight into how the error propagates from the velocity field to the pressure field.

In order to better understand the performance and error properties in the PIV-based pressure calculation, Charonko et al. reviewed and evaluated different factors (i.e., integral method, governing equations, spatial and temporal resolutions, and velocity field smoother etc.) of calculation schemes used in the PIV-based pressure acquisition [3]. Two unsteady synthetic flows with exact solutions and a set of PIV and pressure data from experiments were employed for benchmarking the pressure solvers with various error levels in the velocity fields. In their paper, the authors reported that the Poisson solvers are sensitive to all the aforementioned factors, but to varying levels (the resulting error can vary from less than 1% to more than 100%). They also report that the error in the pressure calculation is highly dependent on the flow type, which implies that there is no optimal method for all flow types. Their study provides several significant contributions to the community (e.g., pressure solver can be very sensitive to the error in the velocity field and the boundary), but it does not provide much rigorous physical or mathematical insight into the error propagation.

In a recent work by Azijli et al., the uncertainty propagation of the PIV-based pressure calculation is discussed in a Bayesian estimation framework [33]. The statistical error profile of the pressure field is estimated based on certain prior knowledge of the velocity field (e.g., divergence free or maximum/minimum of the velocity field), and an assumption that the distribution is Gaussian. Numerical and physical experiments were conducted to validate this Bayesian method, which provide a practical solution for error quantification. However, this method requires prior information of the flow field, and does not provide insight into how the error propagates from the flow field to the pressure calculation.

Here in the following studies, we directly analyze the pressure Poisson equations to unravel the inherent error propagation dynamics of PIV-based pressure calculations: why and how the error in the PIV measurement propagate to the pressure field calculation.

CHAPTER 3. PIV-BASED PRESSURE CALCULATION: IMPLEMENTATION IN A VOCAL FLOW

3.1 Background

Although there have been studies utilizing PIV to resolve the pressure fields of various flows, as described in Chapter 2, very few have applied the technique to voice and glottal flow research. This particular application is intriguing because of the role of airflow in driving vocal fold vibration as well as in the production of audible sound. Oren et al. [34] conducted high-speed, time-resolved PIV on the flow inside canine glottal channels to observe the vortices of the flow in the larynges.

In a follow up study they calculated the pressure field from the velocity fields [35]. To the best of our knowledge, this is the first paper that applied a PIV-based pressure calculation to vocal flow studies. They found that flow separation on the glottal walls happens during closure and creates negative pressure proportional to the subglottal pressure near the folds.

We propose that the error from such a method can be large and that PIV-based pressure measurements require thoughtful consideration before being applied such that errors are reduced sufficiently. The performance of PIV-based pressure calculations are affected by many factors as outlined by Charonko et al. [3] (e.g., pre-processing filters, numerical method, velocity field uncertainties, and temporal/spatial resolution). They emphasize that PIV-based pressure calculations are flow dependent, meaning that each flow type studied may require different methodologies, spatial and temporal resolution, etc.

Thus, in the context of glottal flows, it is necessary to discuss the implications of various conditions and parameters on PIV-based pressure field measurements to ensure that future voice/glottal flow studies utilize the proper settings in experimentation. In this study, recommendations for spatial and temporal resolution as well as best practices are given for performing experiments in the context of glottal folds, with validation from numerical simulations.

3.2 Pressure solver development

3.2.1 Pressure solver

The pressure calculation method involves solving the pressure field from the 2D Navier-Stokes equations supplied with velocities from PIV results. Taking the divergence of the 2D Navier–Stokes equations and assuming the flow is incompressible, the pressure Poisson equation reads,

$$\nabla^2 p = -\rho \nabla \cdot (\boldsymbol{u} \cdot \nabla)\, \boldsymbol{u}, \tag{3.1}$$

where p is the pressure field, $\boldsymbol{u}$ the velocity field, and ρ the density of fluid. To solve the Poisson equation, Neumann boundary conditions (BCs) are applied by rearranging the Navier-Stokes equations,

$$\nabla p = -\rho \left\{ \frac{\partial \boldsymbol{u}}{\partial t} + (\boldsymbol{u} \cdot \nabla)\boldsymbol{u} - \nu \nabla^2 \boldsymbol{u} \right\}, \tag{3.2}$$

where ν is the kinematic viscosity. One advantage of the Neumman BCs is that the viscous effects can be considered by keeping the viscosity term in equation (3.2). Thus, it could provide better results when the viscous force in the flow field is not negligible (e.g., the shear layer of the glottal jet and the air flow within the glottis).

In practice, the Poisson equation with Neumann BCs is solved by the second order finite difference method (five-point scheme discretization in the flow field), and the boundary conditions are evaluated by first order extrapolation. Temporal terms are evaluated by first order forward difference in time. Then the Poisson solver can numerically perform the spatial integration over an $M \times N$ flow field to obtain the pressure field by solving an MN-dimensional linear system, typically $\boldsymbol{A}\boldsymbol{p} = \boldsymbol{f}$, where, $\boldsymbol{A}_{MN\times MN} = A_{i,j}$. $\boldsymbol{p}_{MN\times 1} = p_{i,j}$ and $\boldsymbol{f}_{MN\times 1} = f_{i,j}$ are the pressure and the driving force at each nodal point (i, j), gained by rearranging the nodal points in the domain according to some rearrangement law (for example, the blue arrowhead in figure 3.1 illustrates equation (3.3)):

$$\begin{aligned} \boldsymbol{p}_{MN\times 1} &= [p_{1,1}, \ldots p_{1,M},\ p_{2,1}, \ldots p_{2,M},\ \ldots,\ p_{M,1}, \ldots p_{M,N}]^T \\ &= [p_1,\ p_2,\ \ldots,\ p_k, \ldots,\ p_{MN}]^T. \end{aligned} \tag{3.3}$$

The linear system can then be solved by LU decomposition

$$\boldsymbol{A}\boldsymbol{p} = \boldsymbol{L}\boldsymbol{U}\boldsymbol{p} = \boldsymbol{f}, \tag{3.4}$$

where $\boldsymbol{L}$ and $\boldsymbol{U}$ are lower and upper triangular matrices, respectively. With $\boldsymbol{U}\boldsymbol{p} = \boldsymbol{L}^{-1}\boldsymbol{f}$, and taking advantage of the triangle property of $\boldsymbol{U}$, one can solve the pressure at each nodal point one by one, but in the order $p_{MN}, p_{MN-1}, \ \dots \ p_1$ (as shown by the green integrating path of figure 3.1, which corresponds to the rearrangement law denoted by the blue arrowhead) [1].

One may note that LU decomposition may not be the fastest numerical method, however, it gives clear physical meaning of how the integral is conducted over the whole domain. The solution at one nodal point, $p_{i,j} = p_k$, sums the values of $p_{MN}, \ p_{MN-1}, \ \dots \ p_{k-1}$ as calculated previously on the integral path. This explains the propagation and accumulation of error and/or uncertainty from each PIV data point due to the summation of the error along the path of integration, which can undermine the pressure field estimation.

To overcome this challenge, a common solution is to take advantage of the scalar property of the pressure field, that the pressure values at each location are independent of the integration path. Thus, pressure at each nodal point can be evaluated along multiple arbitrary paths and averaged to remove error. Liu and Katz [32] presented a method that evaluates $10N^2$ paths on an $N \times N$ grid for every pressure point in the flow field, which reduced error. They suggested that 10 paths were necessary for acceptable error levels. Dabiri et al. [4] proposed a more efficient method, using the pressure median of only eight integration paths passing through the point of interest, which yielded relatively accurate results.

In the present research, we use four different integral paths initiating from the four corners of a rectangular flow field by changing the rearrangement law as described in equation 3.3. Two of the four integral paths, which determine the pressure value at the same nodal point, are shown as examples in figure 3.1. The mean calculated pressure value from the four integral paths is treated as the pressure estimation at each nodal point.

The effectiveness of this multi-path estimation technique is validated by a simulation of an unsteady eddy with an analytical solution using a cylindrical tank ($r = 1$ in radius) that initially

[1] p_{MN} must be assigned to a constant (e.g., $p_{MN} = 0$) to make sure an unique solution to $\boldsymbol{U}\boldsymbol{p} = \boldsymbol{L}^{-1}\boldsymbol{f}$ exist.

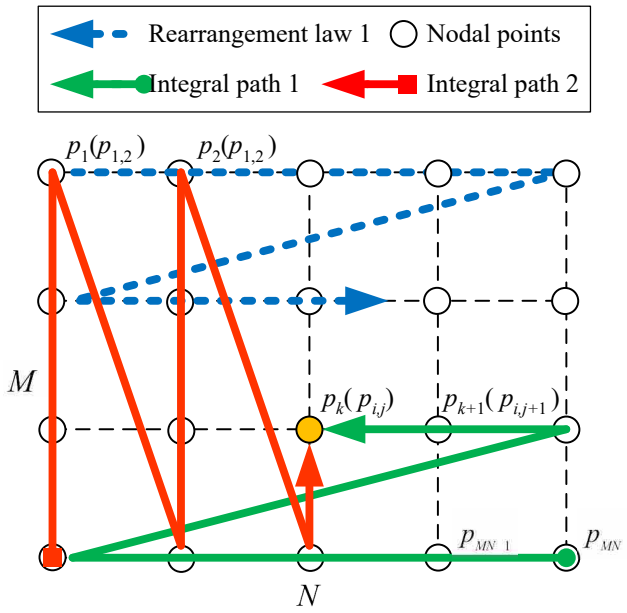

Figure 3.1: Multi-path integration. The pressure at one nodal point, highlighted in orange, is integrated from two of the four different paths.

contains still water. At τ_0 the tank suddenly spins at a constant rotation rate ($\omega = 1$). The velocity and pressure in the flow field then build up gradually from zero until reaching a steady state (i.e., linear velocity profile and parabolic pressure profile along the radius). In polar coordinates, the velocity profile and pressure profile along the radius are

$$V_\theta(r,\tau) = r + \sum_{n=1}^{\infty} \frac{2J_1(\lambda_n r)}{\lambda_n J_0(\lambda_n)} e^{-\lambda_n^2(\tau-\tau_0)}, \tag{3.5}$$

$$p(r,\tau) = \int_0^r \frac{V_\theta(\xi,\tau)^2}{\xi} d\xi, \tag{3.6}$$

where $r \in [0,1]$ and $\tau \in [t_0,\infty)$, ξ is the integral variable, J_0 and J_1 are the Bessel functions of the first kind of zero and first order, respectively, and λ_n are the eigenvalues such that $J_1(\lambda_n) = 0$ [36]. All the variables in equations 3.5 and 3.6 are dimensionless, and the density of the fluid is unity.

3.2.2 Pressure solver validation

The unsteady eddy in the tank described above (section 3.2, equation (3.5) and (3.6)) is utilized to validate the Poisson pressure solver. To study the noise sensitivity of the pressure solver,

the exact solution of the velocity field from equation 3.5 (with or without artificial noise added in the velocity field) is input into the pressure solver to calculate the pressure field and compared with the exact solution of the pressure field (3.6). Noise in the velocity field is modeled by white noise with an amplitude less than 2.5% of the maximum velocity in the flow field. In practice, an inscribed square window is used as the calculation domain inside the cylindrical tank, such that the calculation domain is $\Omega \in [-\sqrt{2}/2, \sqrt{2}/2] \times [-\sqrt{2}/2, \sqrt{2}/2]$. A quiver plot of the flow velocity with zero noise is shown over a color-coded pressure field at a non-dimensional time ($\tau = 0.5$, as defined in equation (3.5) and (3.6)) in figure 3.2.

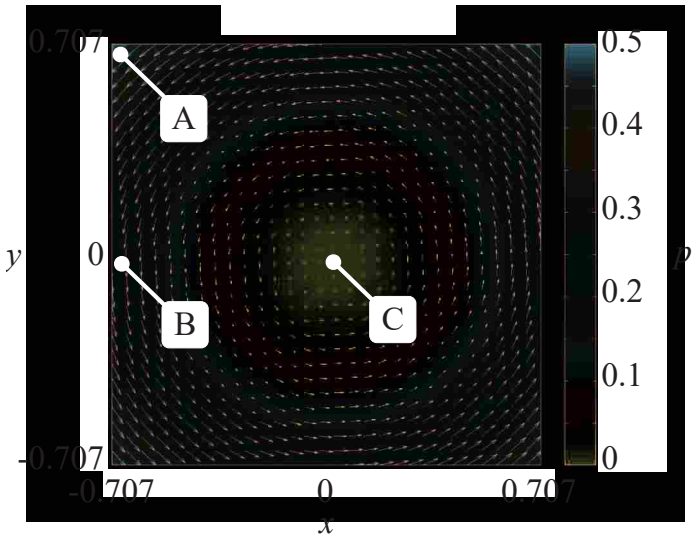

Figure 3.2: Analytical validation: velocity quiver plotted over the pressure field at $\tau = 0.5$. Three locations marked as A, B and C are used as sampling points (see figure 3.3 for the pressure profile vs. time at each location). The entire pressure field is offset to ensure the lowest pressure in the field is zero, which is considered as the reference pressure for convenience.

Three locations (A-C) in the flow domain were selected to show velocity and pressure profiles vs. time in figure 3.3. The simulations show that without added noise in the velocity field, the pressure estimation is nearly identical to the exact solution (approximated by the first 200 terms in the series presented in equation 3.5). This implies that the Poisson solver is reliable. When white noise with less than 2.5% of the amplitude of the local flow velocity was used to model the PIV uncertainties, the Poisson solver propagates and accumulates the error at each nodal point in the flow field. However, the multi-path method reduces the error amplification in the pressure field

calculation indicating that the multi-path method provides a more robust estimate of the pressure field than the single-path method as expected.

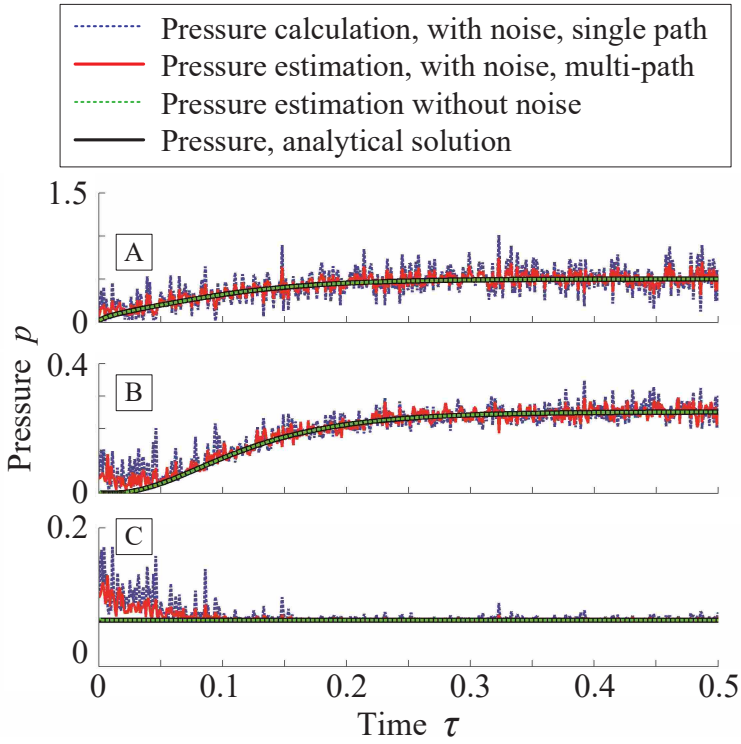

Figure 3.3: Pressure estimation at three locations marked in figure 3.2 as A, B and C. The blue and red lines represent the pressure calculation with and without multi-path integration when a noisy velocity field is applied. The green line indicates the pressure estimation without noise and the black line shows the analytical solutions. As expected the multi-path pressure estimation perform better than the single path integral.

3.3 CFD of 2D Glottal flow

To explore the effectiveness of the Poisson solver in predicting the pressure field in a glottal jet, the solver was applied to the simulated flow field generated by a self-oscillating vocal fold model. The simulation was performed using the commercial finite element software package ADINA using separate but fully-coupled fluid and solid domains to represent the airway and vocal folds, respectively. A summary of the simulation is here presented, noting that other very similar

simulations have been described and reported elsewhere in greater detail [37,38]. Figure 3.6 shows one frame of the CFD result and zoomed view of a region close to the vocal folds.

The fluid domain, representing the airway extending from the subglottic region to the supraglottic region, is shown in figure 3.4. The flow was two-dimensional, laminar, unsteady, and slightly compressible, the latter to allow for acoustic effects to be included [39]. Time marching was accomplished using a 2nd-order, composite method with an integration parameter of 0.7071 and a time step size of 25×10^{-6} sec. The fluid domain consisted of 681,152 4-node flow-condition based interpolation elements (683,838 nodes total). The solution was accomplished using a sparse solver with direct coupling between fluid and solid domains and convergence criteria of 10^{-4}.

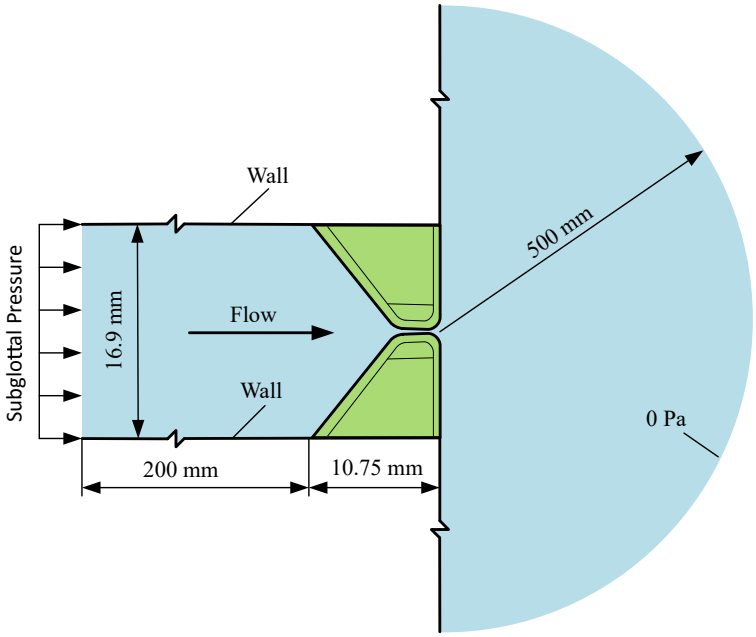

Figure 3.4: Simulation geometry and airway boundary conditions (entrance and exit lengths not to scale).

The solid domain, representing the vocal folds, is illustrated in figure 3.5. Each vocal fold consisted of four layers, representing the epithelium, superficial layer of the lamina propria (SLLP), ligament (intermediate and deep layers of the lamina propria), and body (muscle). The solver allowed for large strain and large deformation. The solid domain consisted of 24,031 9-node quadrilateral elements (97,262 nodes total). Rayleigh damping, with constants $\zeta = 19.8943$ (mass-proportional damping coefficient) and $\eta = 1.253\,23 \times 10^{-4}$ (stiffness-proportional damping

coefficient), was applied to all layers. Each layer had a density of $1070\,\mathrm{kg/m^3}$. The layers were defined using separate Ogden material models with constants obtained by 6th-order curves fit to stress-strain data. The epithelial layer utilized stress-strain data that yielded a constant Young's modulus of 50 kPa. The other three layers' stiffnesses were defined using stress-strain data according to the relationship

$$\sigma = K\left(e^{10.5\xi} - 1\right), \tag{3.7}$$

where ξ and σ denote strain and stress, respectively, and K is a layer-specific constant that governs

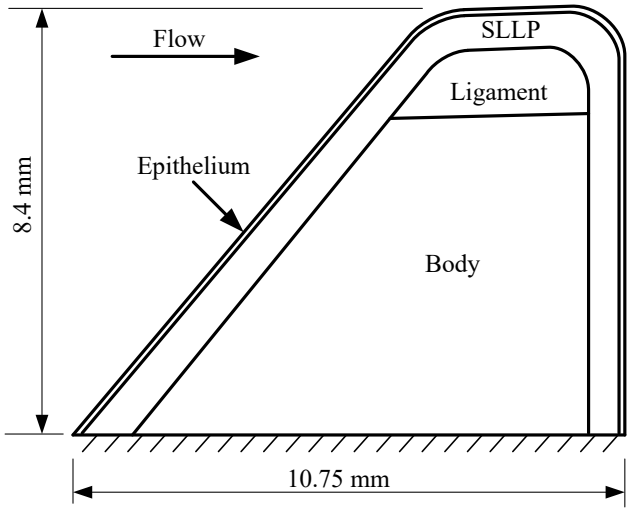

Figure 3.5: Solid domain (vocal fold) geometry.

stiffness, chosen to yield a tangent modulus at 5% strain for each layer (see Table 1, which also includes bulk modulus values for each layer). To prevent the opposing vocal folds from completely closing off the airway, contact planes enforced a minimum gap of 5×10^{-5} m. The initial, pre-vibratory distance between opposing vocal fold models was 1×10^{-5} m.

The unstructured grid from the CFD is then fitted to a regular mesh, a requirement for the pressure solver. The spatial resolution (SR, denoted as $\Delta\, x$) is set to 0.1 mm by an interpolation routine. The temporal resolution (TR, denoted as Δt) of the velocity field is 0.05 ms, also called the sampling rate. The unstructured CFD output are used to provide synthetic PIV results. Figure 3.6 shows one frame of the CFD result and a zoomed-in view of a region close to the vocal folds.

Table 3.1: Vocal fold model material properties.

Layer	Tangent Modulus at 5% strain (kPa)	Constant K (Pa)	Bulk Modulus (kPa)
Epithelium	50	N/A	833
SLLP	0.4	22.535	6.67
Ligament	2	112.677	33.3
Body	25	1408.465	416

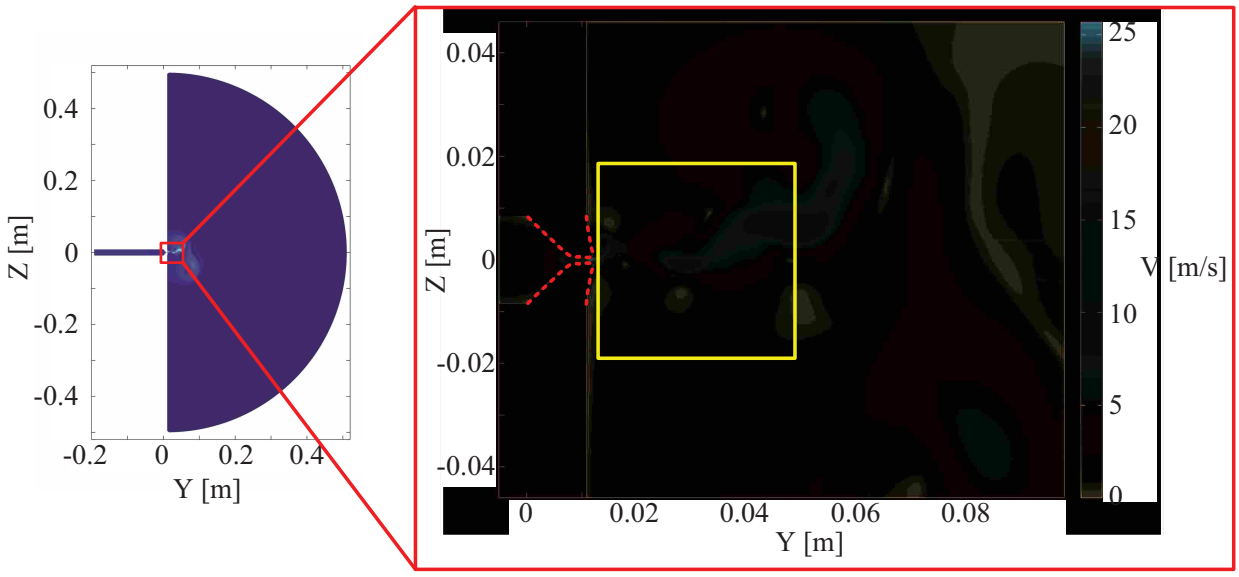

Figure 3.6: Flow field at one time step of the glottal flow simulation, and the zoomed-in view of the area used as calculation domain in this paper (marked by the red box). The red dashed lines marked the profile of vocal folds.

3.4 Results and discussion

3.4.1 Pressure field estimation of intraglottal flow

This section applies the multi-path pressure Poisson solver to a numerically simulated intraglottal flow. One oscillation cycle during the numerical simulation is shown in figures 3.7–3.9 (presented in section 3.3). In this section, the pressure data is normalized by the inlet pressure ($p_{in} = 900$ Pa), the temporal data by the oscillation period of the vibrating vocal folds ($T = 4.2$ ms), and the spatial data by the glottal width at maximum flow rate ($L = 0.896$ mm). All the non-dimensional variables are denoted by superscript (*).

Figure 3.7 shows the 2D flow rate ($q^* = qT/L^2$, where, q is the flow rate calculated from the CFD model) though the vocal folds versus non-dimensional time ($t^* = t/T$) with time-stamp ($t^* = 0.512$) marked by a red circle (2.15 ms from the beginning of the cycle).

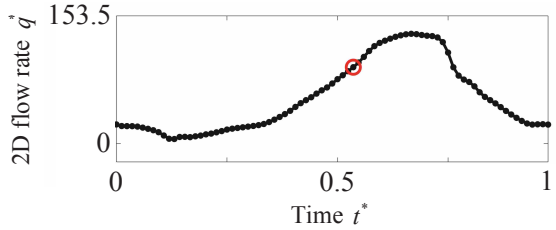

Figure 3.7: 2D flow rate though vocal folds in one cycle. Red circle marks $t^* = 0.512$ reported in figure 3.8.

Limitations of the present method include an inability to estimate reasonable data at the solid-fluid boundary. The Poisson solver is sensitive to the boundary conditions with a high uncertainty level in the velocity field near any boundary, which would ruin the pressure calculation throughout. It is reasonable to avoid involving walls in common PIV practice because reliable PIV measurements close to the wall are naturally challenging due to the large flow gradient near the wall and complicated particle seeding techniques [40]. Therefore, we chose a fixed window (4 cm$\times$4 cm) within the supra-glottal channel as the calculation domain (outlined in figure 3.6). This domain is as close as possible to the vocal folds but without contacting the vocal folds during the oscillation cycle.

Figure 3.8 shows the velocity, pressure fields from the CFD simulation of glottal flow at $t^* = 0.512$ in the cycle shown in figure 3.7, and the pressure estimation as well as the errors. The velocity field from the CFD simulation is used as the input (shown in figure 3.8(a)) to the Poisson solver. The non-dimensionalized gauge pressure field ($p^* = (p - \bar{p})/p_{in}$) is shown in figure 3.8(b), where, p is the pressure field from CFD simulation, $\bar{p}$ the mean pressure in the domain; and the length scales are normalized as $y^* = Y/L$ and $z^* = Z/L$. The multi-path integration is used to estimate the pressure field (denoted as $\hat{p}$). The normalized pressure field estimation $\hat{p}^* = (\hat{p} - \bar{\hat{p}})/\bar{p}_{in}$ is shown in figure 3.8(c), where $\bar{\hat{p}}$ is the mean estimated pressure.

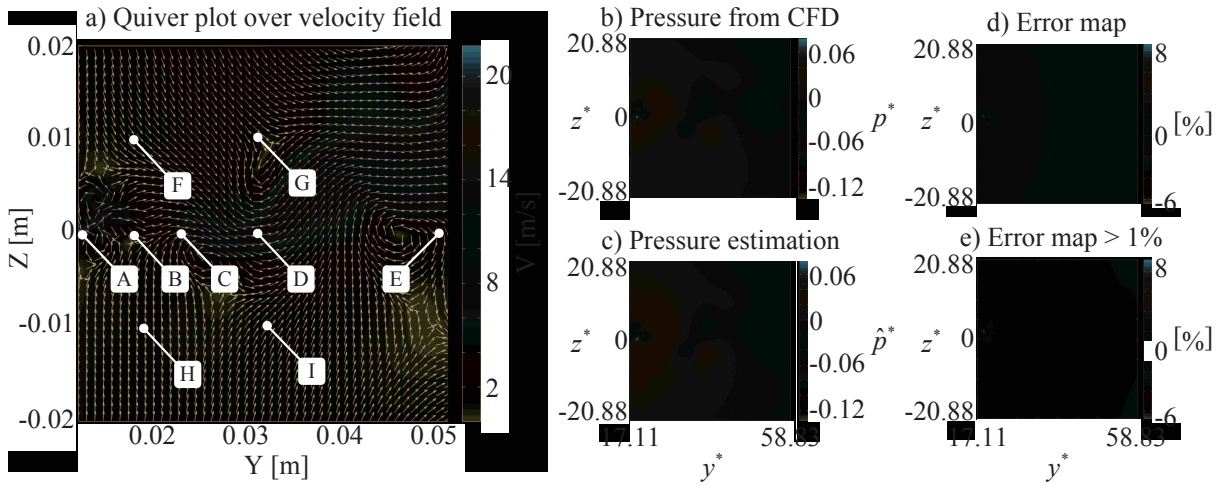

Figure 3.8: Simulation at $t^* = 0.512$. a) Vectors plotted over velocity field contours representing the input for the pressure estimation. b) Normalized pressure field obtained from CFD. c) Normalized pressure estimation, p^*, from the Poisson solver. d) Relative error map of normalized pressure field. e) Relative error map of normalized pressure larger than 1% (9 Pa).

To calculate the relative error map, the absolute pressure error is divided by the constant inlet pressure as presented in figure 3.8(d). Figure 3.8(e) shows the error map where the relative error is larger than 1%, which corresponds to 9 Pa.

Figure 3.9 shows the pressure values from the CFD simulation compared with our estimated values versus time at nine locations marked as A-I in figure 3.8. Pressure estimations agree with the pressure values from CFD at each location, but errors are relatively larger at location A, especially after $t^* = 0.5$. These pressure errors may be due to errors propagated from the velocity field through the Poisson solver, which is introduced by interpolation, typically, in the area nearest to the fluctuating walls (the mesh in the area close to the vocal folds is much finer than the grid spacing used for interpolation). The pressure estimation generally responds faster than the pressure from CFD in time. This may stem from the fact that the sampling rate is not high enough to resolve the flow field. However, we note that these temporal fields are already as high as state-of-the-art high-speed time resolved PIV systems ($\Delta t = 0.05$ ms).

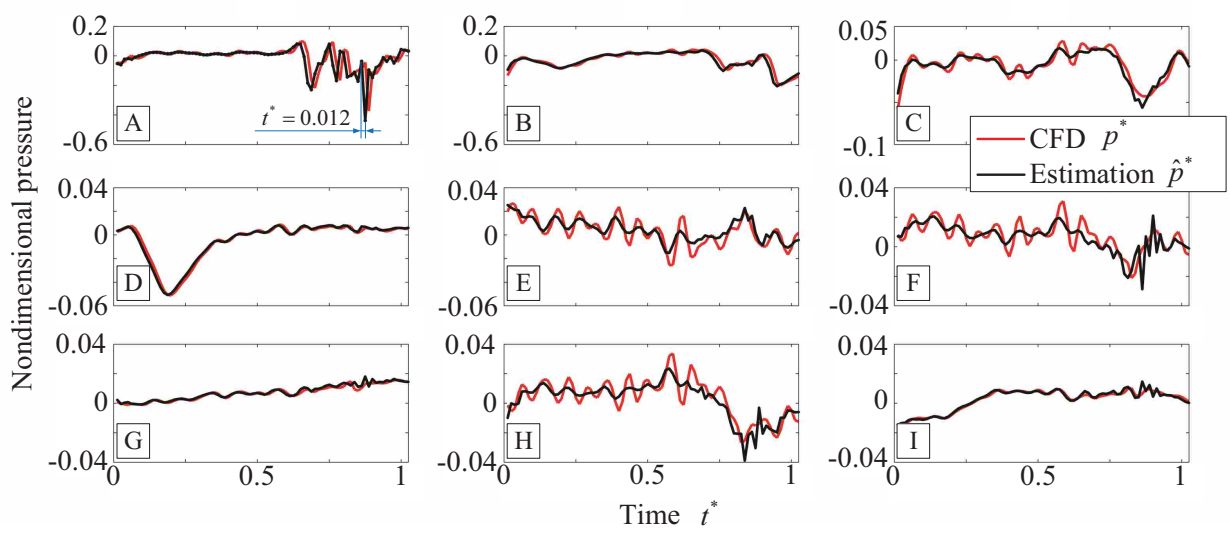

Figure 3.9: Nondimensional pressure versus nondimensional time at nine locations (A-I as marked in figure 3.8)

3.4.2 Practical recommendations for PIV resolutions

We now present practical estimations for PIV spatial and temporal resolutions needed for estimating pressure. The error in the pressure estimation versus temporal and spatial resolutions are shown in figure 3.10. This computation is accomplished by interpolating the CFD simulation velocity data with different step sizes as inputs to the synthetic PIV data with different spatial resolution (SR, $\Delta x = 0.05,\ 0.1,\ 0.3,\ 0.5,\ 1$ mm) and time resolution (TR, $\Delta t = 0.05,\ 0.1,\ 0.2,\ 0.4,\ 0.8,\ 1.6$ ms); the non-dimensionalized SR and TR are $\Delta x^* = \Delta x/L$ and $\Delta t^* = \Delta t/T$, respectively. To evaluate the performance of the pressure estimation, the spatial-averaged non-dimensional mean error (e^*, termed hereafter as mean error) measured at t^* is ,

$$e^*(t^*) = \frac{1}{|\Omega|}\int_\Omega |\left(\hat{p}^* - \hat{\bar{p}}^*\right) - \left(p^* - \bar{p}^*\right)| \mathrm{d}\Omega, \tag{3.8}$$

where $|\Omega|$ is the area of the domain Ω (presented as box plots in figure 8). This area can be the whole flow domain (e.g. figure 3.10(O)), or a small window (1 mm $\times$ 1 mm) at specific locations (e.g figure 3.10 (A, C, and D)).

Figure 3.10(O) shows the normalized mean error in the whole flow field covering the 4 cm $\times$ 4 cm calculation window. The red bar inside each box marks the median of the data set. The cir-

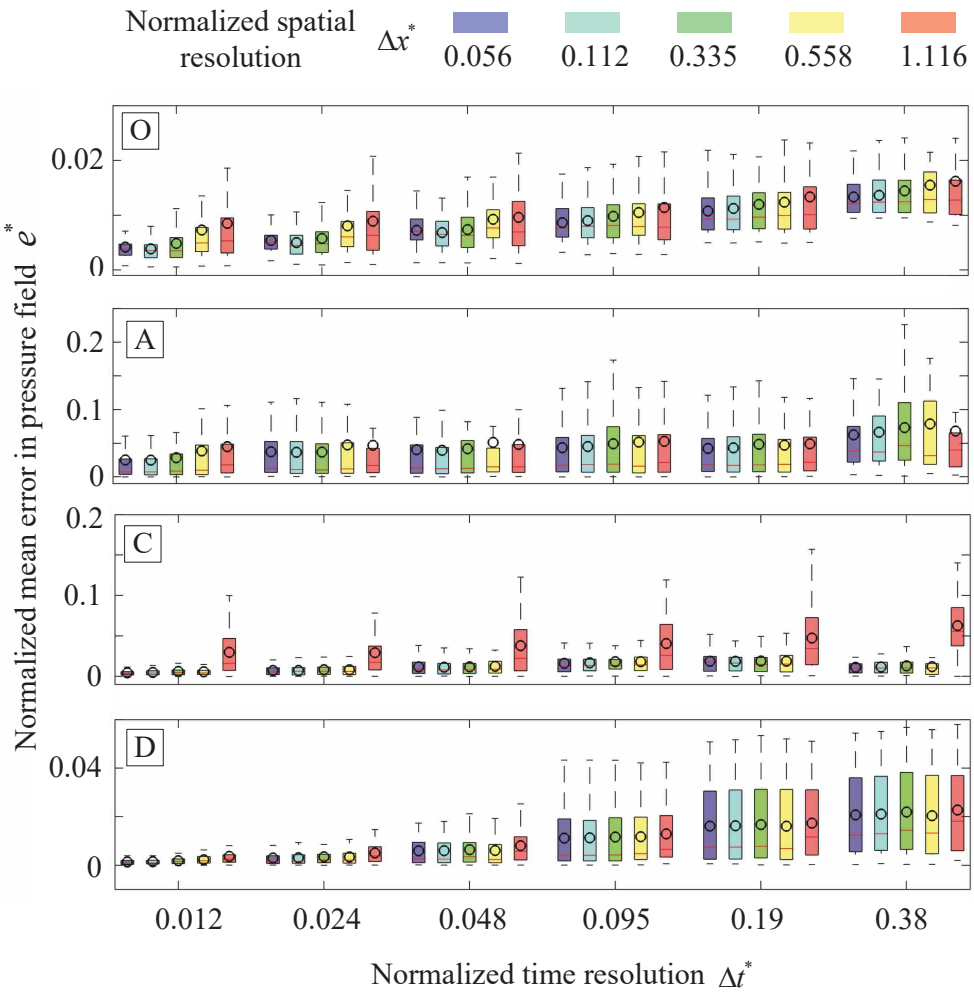

Figure 3.10: Grouped boxplot of mean error at different SR and TR. (O) mean error of whole flow field. (A, C and D) mean error in a 1 mm $\times$ 1 mm window at locations A, C and D (figure 3.8

cles mark the time-averaged mean error, which is $e^* = \frac{1}{T}\int_0^T e^*(t)\mathrm{d}t$. The upper and lower whiskers confine the data set within a 99.7% confidence interval. The upper and lower limits of the boxes are the 75% and 25% percentile, respectively. Each box contains 83 to 36 data points (time averaged mean error) depending on the TR. For the whole flow field $\Delta x^* \geq 0.558 \cup \Delta t^* \geq 0.048$ yields relatively higher upper whisker and higher mean value than other SR and TR settings.

The mean error at location A in the flow field (marked in figure 3.8) covers a 1 mm $\times$ 1 mm window, as shown in figure 3.10(A). At location A (see figure 3.9) the pressure changes can be extremely fast from about 0 to -0.4 in 0.012 dimensionless time units; thus location A can be considered a typical high frequency area of the flow. In practice, we suggest that plots similar to

figure 3.10 be used as look-up tables to determine appropriate resolution settings to balance the cost of PIV setup and quality of pressure estimation. For example, based on the simulations in this research $\Delta x^* \leq 0.335 \cap \Delta t^* \leq 0.012$ is recommended to ensure normalized mean error is less than 0.1 when the flow field fluctuates rapidly near the vocal folds. However, we have limited our estimation of reasonable normalized mean error to no larger than 0.1 which for the pressures within the simulation ($P_{in} = 900$ Pa) is 90 Pa. This may not be acceptable in some practical estimations and may therefore necessarily need to be set lower.

Figure 3.10(C) shows results similar to 3.10(A) but sampled at location C in the flow field (figure 3.8(A)). Location C is only 1 cm away from A; but the results differ significantly. The jet has dissipated in this area, such that the flow has lower frequency, and consequently a higher tolerance in TR and SR. We consider location C and further places from the base of the glottal jet (e.g., location D in figure 3.8(a)) as low frequency areas. It is evident that some refinement must be applied to get the fidelity necessary for these specific cases, however, as the fluctuations decrease in frequency the TR necessary to gather reasonable pressure data increases. In addition, when the SR is large ($\Delta x^* \geq 1.116$), the mean error at C increases significantly. This may be due to the low-pass-filter-like properties of the Poisson solver, [21, 41]. While the high frequency dynamics, although important, are filtered out substantially.

Figure 3.10(D) presents results at location D, which is in the middle of the flow field (see figure 3.8). In this region, the mean error is small in general compared to other locations (i.e. A and C). For example, even the coarsest resolution we tested ($\Delta x^* \leq 1.116 \cap \Delta t^* \leq 0.38$) led to normalized mean error less than 0.06.

We noticed that sometimes a fine resolution (either TR or SR) did not always lead to lower error. For example, in (O) and (A) of figure 3.10, $\Delta x^* = 0.112$ yields the best performance in terms of time averaged error, rather than finer meshes. This non-intuitive phenomena may be caused by over-sampling of the noise by fine meshes and/or amplification of noise due to small grid-spacing used in the difference scheme. A similar phenomenon is discovered by [3] with numerical simulation, and also analyzed by several papers such as [1, 21].

In previous studies based on pressure calculation from PIV data, we find that the spatial and/or temporal resolutions of the PIV experiments may not be enough to accurately resolve an accurate pressure field. For example, Oren et al. [34, 35] operated the camera at a 5 kHz sampling

rate, with each image pair separated by 3.0 μs. The high-speed images had a spatial resolution of 83 pixel/mm and were processed using an adaptive interrogation window (64×64 to 32×32) with 75% overlap. Outliers in the velocity vectors were filtered such that the spatial resolution was reported as 0.2892 mm. In addition, the minimum particle displacements of $1/4$ of a pixel were removed as well as maximum displacements of $1/4$ of the window size, which could introduce systematical bias to the PIV results. Even if the error in the experiments by Oren et al. [35] is as low as the synthetic flow used in our studies, which is mainly from interpolation, the resolution used by Oren et al. [35] is barely enough to obtain results with reasonably small errors. As a side reference, a PIV-based pressure calculation of a jet in a diffuser with fixed walls (which could be considered as a similar but less challenging flow than vocal flow) with high quality PIV reported by Charonko et al. [3] shows that even when a conservative pressure Poisson solver is used, the error on the wall can be as high as 75% compared to the inlet kinetic pressure. However, the mixed boundary conditions used by Oren et al. [35] may improve the tolerance of the pressure solver to the PIV resolution as well as the uncertainties near the walls, and lead to acceptable pressure field estimations (refer to chapter 4 for the detailed discussion of the influence of the boundary conditions on the error propagation). Nevertheless, we still recommend using high resolution PIV settings and multi-path integral methods (e.g. [32] and [4]) to reduce the error in the pressure calculation, especially when validation is not available.

3.5 Discussion

As Charonko [3] suggested, for PIV-based pressure estimations, proper temporal and spatial resolution, specific to the flow field, are vital to obtain meaningful data. Herein, specific considerations for vocal fold flow field pressure estimations are presented. Not surprisingly, it is shown that coarser resolutions (e.g. $\Delta x^* \geq 0.558 \cup \Delta t^* \geq 0.048$ for overall acceptable performance in the whole flow field) yield larger error in pressure estimations due to the loss of flow information from the low resolution. In reality, however, PIV systems have limitations, especially with regards to spatial resolution (e.g., our in-house system yields SR=0.3 mm and TR=0.2 ms, $\Delta x^* = 0.335$ and $\Delta t^* = 0.0476$ if normalized). These limitations may decrease confidence in obtaining reliable pressure estimates using this method. For instance, the fast changing flow in a glottal channel (position A in figure 3.8 which is very close to the vocal folds) may require time and spatial resolution

beyond the capabilities of a common PIV system. In order to relax the SR and TR requirements, we suggest either to pay attention to PIV experiments, such as proper lighting, particle seeding, and filters in post-processing to reduce the uncertainties of velocity field; and/or use a pressure solver that averages pressure values calculated from many different integral paths (e.g. [32]) to take fully advantage of the scalar property of the pressure field and consequently reduce the sensitivity to the noise in the velocity field.

However, too fine of a mesh may amplify the noise through the numerical algorithm; for example, the viscous term of equation (3.2) is evaluated numerically as

$$\nabla^2 u_{i,j} = \frac{\rho \nu}{\Delta x^2} \left(u_{i+1,j} + u_{i-1,j} + u_{i,j+1} + u_{i,j-1} - 4u_{i,j} \right). \tag{3.9}$$

Thus, $\nabla^2 u \sim \Delta x^{-2}$. The velocity data at each nodal point could be contaminated by noise from experiments (i.e., $u_{i,j}$ actually has experimental error in it). Fine resolution (small Δx and/or Δt) could reduce numerical error from the numerical scheme, however, it may increase the experimental error by amplifying the noise in the velocity field. For example, $\Delta x^* = 0.056 \cap \Delta t^* = 0.012$ is not the best resolution setting, although it is the finest mesh we examined herein, as shown in the first three groups of box-plots in figure 3.10(O) and the third group in figure 3.10(D).

Positions A, C, and D in the flow field (figure 3.8) are spaced 1 to 3 cm apart downstream of the vocal jet, however, the pressure estimation in these locations is significantly different. Moreover, the error boxes in figure 3.10 are tall in general. These observations are not surprising, given that the PIV-based pressure estimation is flow dependent and sensitive to the error in the velocity field as argued by Charonko et al. [3].

Thus, in addition to considering the complicated characteristics of the PIV-based pressure calculation, and the resolution recommendations based on the 2D simulation we have presented, we also suggest that for each experimental data set, simulations related to the experiments be used to find reasonable PIV parametric settings before starting.

CHAPTER 4. ERROR PROPAGATION DYNAMICS

4.1 Introduction

The work presented in chapter 3 is not only an example of an application of the PIV-based pressure solver using vocal flow, it is also a numerical validation and support to the work of Charonko et al. [3]. We confirmed that the PIV-based pressure calculation, specifically the pressure Poisson equation based method, is potentially unreliable and can be affected by several factors including:

- Error level and grid resolution of PIV data
- Flow type
- Calculation scheme (including filters, governing equations etc)
- Boundary condition settings

It is not intuitively difficult to accept that the factors listed above affect the pressure calculation, however, *why* and *how* these factors matter remains unclear. Very little research has been done to investigate the dynamics of error propagation from PIV-based velocity measurements to the pressure field calculation.

In this chapter, the dynamics of the error propagation are investigated by examining the Poisson equation directly, rather than through experimental means. The error bound in the pressure field is analytically quantified and the mathematical roots of why and how the Poisson equation based pressure calculation propagates error from the PIV data is illustrated.

First, the error-contaminated Poisson problem raised by the pressure field calculation from noisy PIV experiments is clearly specified. In section 4.2 and 4.3 this engineering problem is translated into an applied mathematical problem, specifically by obtaining bounds on solutions of the Poisson equation. In section 4.4, rigorous bounds are presented on the error in the pressure

calculation relative to the error inherent from the PIV measurements. Several typical examples are provided. In section 4.5, the limitations and practical uses of this work are discussed.

4.2 Problem statement

In general, there are two classes of schemes used to calculate a pressure field from velocity field: i) directly integrating the pressure gradient derived from the Naiver-Stokes equation (e.g., Liu and Katz [32]); ii) solving the pressure Poisson equation (e.g., de Kat and van Oudheusden [21]), which is more commonly used. Here, I focus on how the error in the velocity data propagates to the pressure field through the latter scheme.

Rearranging the incompressible non-dimensionalized Naiver-Stokes equation and applying divergence on both sides, the pressure Poisson equation reads

$$\nabla^2 p = -\nabla \cdot \left(\frac{\partial \boldsymbol{u}}{\partial t} + (\boldsymbol{u} \cdot \nabla \boldsymbol{u}) - \frac{1}{Re} \nabla^2 \boldsymbol{u} \right) = f(\boldsymbol{u}) \qquad in\ \Omega, \tag{4.1}$$

where p is the pressure field, $\boldsymbol{u}$ denotes the velocity field, Ω is the flow domain, and Re is the Reynolds number. When Re is large, the viscous term can be neglected [1,21]. The vector function (f) of the velocity field ($\boldsymbol{u}$) is called data (to avoid confusion, in this dissertation "data" is used as the term for the right hand side of a Poisson equation and its boundary conditions). With certain boundary conditions, for example,

$$p = \frac{1}{2} \left(\boldsymbol{u}^2 - \boldsymbol{u}_\infty^2 \right) = h(\boldsymbol{u}) \qquad on\ \partial\Omega, \tag{4.2}$$

and/or

$$\nabla p \cdot \boldsymbol{n} = -\frac{\partial \boldsymbol{u}}{\partial t} - (\boldsymbol{u} \cdot \nabla \boldsymbol{u}) + \frac{1}{Re} \nabla^2 \boldsymbol{u} = g(\boldsymbol{u}) \qquad on\ \partial\Omega, \tag{4.3}$$

the pressure field can be found by solving (4.1). Here h and g are the data on the Dirichlet boundary (typically applied to the steady irrotational region of a flow with Bernoulli's equation, especially in the far field) and Neumann boundary (commonly used on a wall boundary), respectively, which are both functions of the velocity.

In engineering practice, experiments always introduce systematic bias and/or random errors, which are usually unknown and thus called uncertainties in the PIV community. These uncer-

tainties will lead to a contaminated pressure calculation (denoted by $\tilde{p}$). The uncertainties in the pressure calculation are also unknown, which can cause even more frustration. Regardless of the physical meaning, this dissertation will refer to uncertainties as error for convenience. If the error in the data of the pressure Poisson equation is denoted as ϵ_f, then $\tilde{p}$ solves the equation with the error included

$$\nabla^2 \tilde{p} = f(\boldsymbol{u}) + \epsilon_f \qquad \textit{in } \Omega. \tag{4.4}$$

Similarly, $\tilde{p}$ satisfies the error-contaminated boundary conditions:

$$\tilde{p} = h(\boldsymbol{u}) + \epsilon_h \qquad \textit{on } \partial\Omega, \tag{4.5}$$

and/or

$$\nabla \tilde{p} \cdot \boldsymbol{n} = g(\boldsymbol{u}) + \epsilon_g \qquad \textit{on } \partial\Omega, \tag{4.6}$$

where, ϵ_h and ϵ_g are the error on the Dirichlet and Neumann boundaries, respectively.

Based on this problem statement, we aim to answer a question rising from engineering practice — *Question 1: How do the errors from the experimental results ϵ_f, ϵ_h and/or ϵ_g affect the errors in the contaminated pressure field $\tilde{p}$?*

4.3 Modeling the error propagation

We now present how to translate from an engineering problem (*Question 1*) to a tractable applied mathematical question (*Question 3*, see below).

We consider ϵ_f, ϵ_h and ϵ_g as perturbations to the data of the Poisson equation. Perturbing the data ($f, g,$ and/or h) is mathematically equivalent to propagating error from the data to the pressure field. This means that *Question 1* can be rewritten as — *Question 2: Does the solution p continuously depend on the data $f(\boldsymbol{u})$, $g(\boldsymbol{u})$, and/or $h(\boldsymbol{u})$, and if so, then how?*

Assuming the uncertainty contaminated pressure field can be separated as $\tilde{p} = p + \epsilon_p$, where ϵ_p is the error in the calculated pressure field, and taking advantage of the linear property of the Laplace operator and subtracting equation (4.1) from (4.4) leads to

$$\nabla^2 \epsilon_p = \epsilon_f \qquad \textit{in } \Omega, \tag{4.7}$$

which is a Poisson equation with respect to the error in the pressure field. Similarly, the boundary conditions read

$$\epsilon_p = \epsilon_h \qquad on\ \partial\Omega, \tag{4.8}$$

and/or

$$\nabla\, \epsilon_p \cdot \boldsymbol{n} = \epsilon_g \qquad on\ \partial\Omega. \tag{4.9}$$

Since the error in the data (ϵ_f, ϵ_h, and ϵ_g) are unknown, it is not expected to calculate the error at every specific location in the pressure field (ϵ_p). However, it is possible to estimate the average *error level* of the pressure field over the entire domain with equation (4.7), (4.8) and (4.9). To measure the level of the error, we define the L^2 norm in a domain, for example the error level in the pressure field as

$$|| \epsilon_p ||_{L^2(\Omega)} = \sqrt{\frac{\int \epsilon_p^2 \, d\Omega}{|\Omega|}}, \tag{4.10}$$

where $|\Omega|$ is the length, area or volume of the domain, depending on the dimension of the flow field. In physical terms, the L^2 norm defined in equation (4.10) measures the power of the errors per unit space, and thus is given the term "error level" hereafter. In addition to the L^2 norm, the L^∞ or sup norm is also used here and defined by:

$$\|f\|_{L^\infty(\Omega)} = \sup_{x\in\Omega} |f(x)|. \tag{4.11}$$

With the defined error level, *Question 2* can be transformed into — *Question 3: Whether and how* $|| \epsilon_p ||_{L^2(\Omega)}$ *is bounded by* $|| \epsilon_f ||_{L^2(\Omega)}$, $|| \epsilon_g ||_{L^2(\partial\Omega)}$, *and/or* $|| \epsilon_h ||_{L^2(\partial\Omega)}$ *for the Poisson problem given by equation (4.7), (4.8), and/or (4.9)?*

From *Question 1*, to *2*, and then *3*, we have been able to transform a typical engineering problem to a well defined applied mathematical one: estimate the bounds of the solution to a Poisson boundary value problem (BVP) with respect to ϵ_p, which is actually a measure of the error in the pressure field.

4.4 Bounds on error

In this section it is shown that the error level can be bounded in the pressure field, given the i) geometry and ii) scale of the domain, iii) type of the boundary conditions, as well as the iv) error level in the data (in the field and on the boundary) utilizing the Poincare and Cauchy-Schwartz inequalities (see A for details). The results are independent of the numerical scheme of the Poisson solver, i.e. the choice of the numerical scheme may introduce additional errors not accounted for in the present analysis. The results are general and thus work for any dimension of the domain (i.e., two-dimensional(2D) or three-dimensional(3D) flow).

Bounds on the error for several cases with different boundary condition settings are discussed. These cases are not only typical in engineering practice but also convenient for unveiling the mathematical insights of the error propagation dynamics. Within each case study, the analytical results will be validated with numerical simulations first. Then the dynamics of the uncertainty propagation through the pressure Poisson equation will be discussed based on analysis from a flow field with more general geometry (i.e., rectangular). Finally, the physical interpretation of the mathematics and suggestions for engineering practice are addressed.

4.4.1 Dirichlet boundary case

Consider a domain with pure Dirichlet boundary condition, the error in the pressure field can be bounded as

$$|| \epsilon_p ||_{L^2(\Omega)} \leq C_D || \epsilon_f ||_{L^2(\Omega)} + || \epsilon_h ||_{L^\infty(\partial\Omega)}, \tag{4.12}$$

where C_D is the Poincare constant, which is related to the minimum positive eigenvalue of the Laplace oprator in the specified domain. Specifically, in engineering practice, the value of the Poincare constant is determined by the dimension, size, and shape of the domain, as well as the type of boundary conditions (A.3).

To validate inequality (4.12), we consider a steady 2D potential vortex in an $L \times L$ domain in Cartesian coordinates. The nondimensionalized velocity field is $u = -y$, $y \in (-L/2, L/2)$; $v = x$, $x \in (-L/2, L/2)$, where u and v are the two components of the velocity field $\boldsymbol{u}$ in the x and y direction, respectively (see figure 4.2). Thus the pressure field is $p = (x^2 + y^2)/2$. The Dirichlet

boundary conditions are defined as $p = (y^2 + L^2/4)/2$, $x = \pm L/2$, and $p = (x^2 + L^2/4)/2$, $y = \pm L/2$.

Artificial errors are constructed for the data. To test the reliability of the underlying estimate, we consider a uniformly constant error, $\epsilon_f = 2^{-4}$, and $\epsilon_h = 2^{-4}$. The error level in the domain and on the boundary is specified identically ($|| \epsilon_f ||_{L^2(\Omega)} = || \epsilon_h ||_{L^\infty(\partial\Omega)} = 2^{-4}$). Assuming the uncertainty in the data is constant is beneficial in two ways. First, in a physical sense, constant uncertainty is associated with systematic error (i.e., $\epsilon_f = 2^{-4}$ could be equivalent to $u = -(1-2^{-6})y$ and $v = (1-2^{-6})x$ for the steady potential vortex used here). The systematic error is most likely from slightly inaccurate calibration in real experiments, and can introduce considerable error in the data and consequently accumulate even more error in the pressure field. Second, a constant error field will lead to a constant error level, which will make the later analyses explicit.

We numerically solve the pressure Poisson equation with artificial error introduced (4.4), using an accurate second order (five point scheme with point-wise numerical error less than 8.2×10^{-12}) finite difference Poisson solver (similar to Reimer et al. [42]). The error in the pressure field from the simulation is then compared with the analytical results inequality (4.12). We expect that the error from numerical simulations will be less than the prediction in (4.12), but generally follow similar trends. If the errors from the numerical simulations are close to the analytical prediction (i.e., slope and value), we say inequality (4.12) is validated and the bound is sharp.

For the 2D square Dirichlet domain, the Poincare constant is $C_D = L^2/2\pi^2$, and inequality (4.12) becomes

$$|| \epsilon_p ||_{L^2(\Omega)} \leq \frac{1}{2\pi^2} L^2 || \epsilon_f ||_{L^2(\Omega)} + || \epsilon_h ||_{L^\infty(\partial\Omega)}. \tag{4.13}$$

Figure 4.1 shows the comparison of numerical simulations and the analytical prediction. The numerical simulations are conducted based on equations 4.4 and 4.5, with the 2D potential vortex as the flow field and the constant artificial errors (introduced in the pressure Poisson equations in the field only (blue squares); on the boundary only (red triangles); and both in the field and on the boundary (black open circles)). Inequality (4.13) is represented by a black solid line and is the upper bound of the error. Clearly inequality (4.13) fits well with the simulation results when error is introduced to both the field and boundary.

In figure 4.1, when the length scale of the domain is large the uncertainty level in the pressure field is dominated by the error of the data in the field (blue squares are collapsed on black open circles), and proportional to the area of the domain ($|| \epsilon_p ||_{L^2(\Omega)} \sim L^2$). When the domain is small, the error in the pressure field is dominated by the error on the boundary (red triangles are collapsed on black open circles), and independent of the length scale of the domain ($|| \epsilon_p ||_{L^2(\Omega)} \sim L^0$). Intuitively this makes sense as smaller domains will be more influenced by their boundaries.

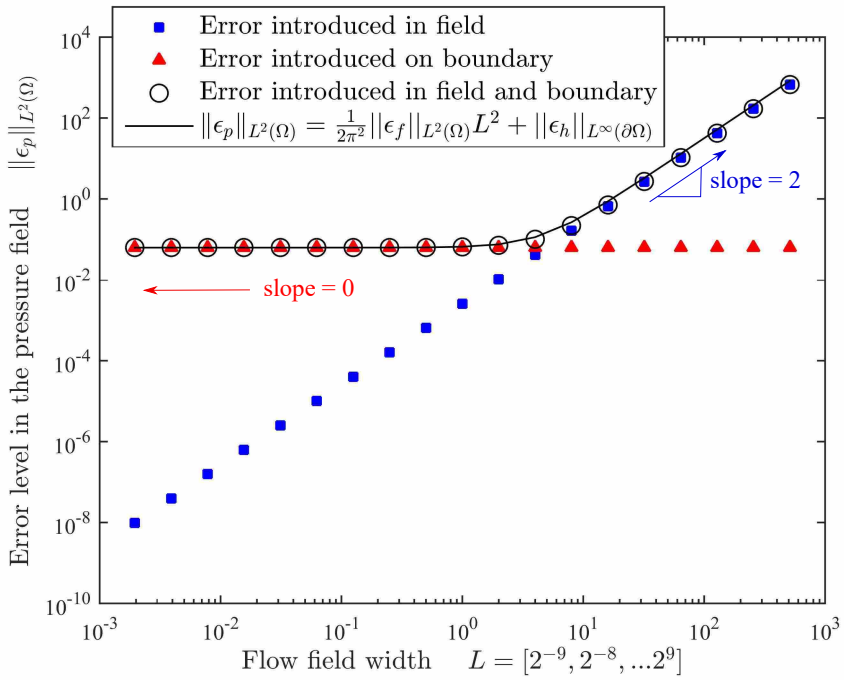

Figure 4.1: Error level in the pressure field versus the width of the flow field for the Dirichlet case. The data points illustrate the error level when artificial error is introduced in the field only (blue square), on the boundary only (red triangle), and both in the field and on the boundary (black open circle). The black solid line is the bound of the error of the pressure field based on inequality (4.13).

When conducting PIV experiments, if the frame rate of the camera is fixed, one can customize the aspect ratio of the video, but the area of the interrogation windows is usually about the same due to best practices and the limitations of lighting and magnification (e.g., best practices of particles per pixel, particles per interrogation window, number of pixels of motion per time step, etc.). Thus, from an engineering perspective, it is important to discuss how to choose the aspect

ratio when the number of pixels of the video is fixed. In order to study this physically, we vary the shape of the domain (alter the aspect ratio of only a rectangular shape due to physical restraints of the camera) to see how the error propagation dynamics is affected when the area of the domain is fixed.

Considering a 2D $N \times M$ rectangular domain (Fig.4.2), inequality (4.12) leads to:

$$|| \epsilon ||_{L^2(\Omega)} \leq \frac{\alpha}{\pi^2(1+\alpha^2)} A || \epsilon_f ||_{L^2(\Omega)} + || \epsilon_h ||_{L^\infty(\partial\Omega)}, \tag{4.14}$$

where α is the aspect ratio ($\alpha = N/M$) of the domain, and A is the area of the domain ($A = MN$). Given the error level in the data, one can use inequality (4.14) to estimate the error level in the pressure field. If necessary, one can also adjust the parameter settings (aspect ratio and/or area of the domain) to reduce the error propagation.

Figure 4.3 illustrates how the aspect ratio and area of the domain affect the error propagation (assuming the uncertainty level of data is $|| \epsilon_f ||_{L^2(\Omega)} = || \epsilon_h ||_{L^\infty(\partial\Omega)} = 2^{-4}$). For each curve (fixing domain area A), the maximum appears at $\alpha = 1$, which means a square PIV window is the worst case scenario if a Dirichlet boundary condition is applied. When the domain is elongated (e.g., $\alpha \to 0$) and pressure on the boundary is known, the pressure field is mainly determined by the Dirichlet boundary conditions on the longer edges, and the contribution of the error in the field and the shorter edges becomes negligible. Thus, using an elongated flow field (α far from 1) is encouraged when precise boundary conditions (accurate measurements on boundaries) are accessible, especially on the long edges.

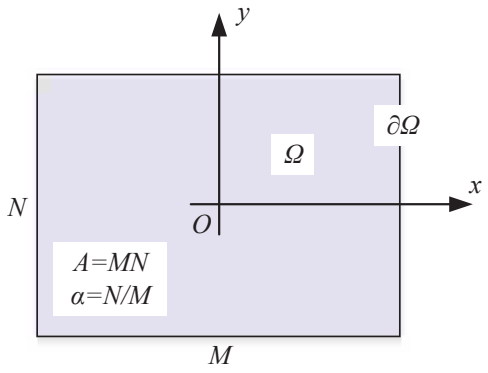

Figure 4.2: $N \times M$ Domain Ω with aspect ratio α and area A.

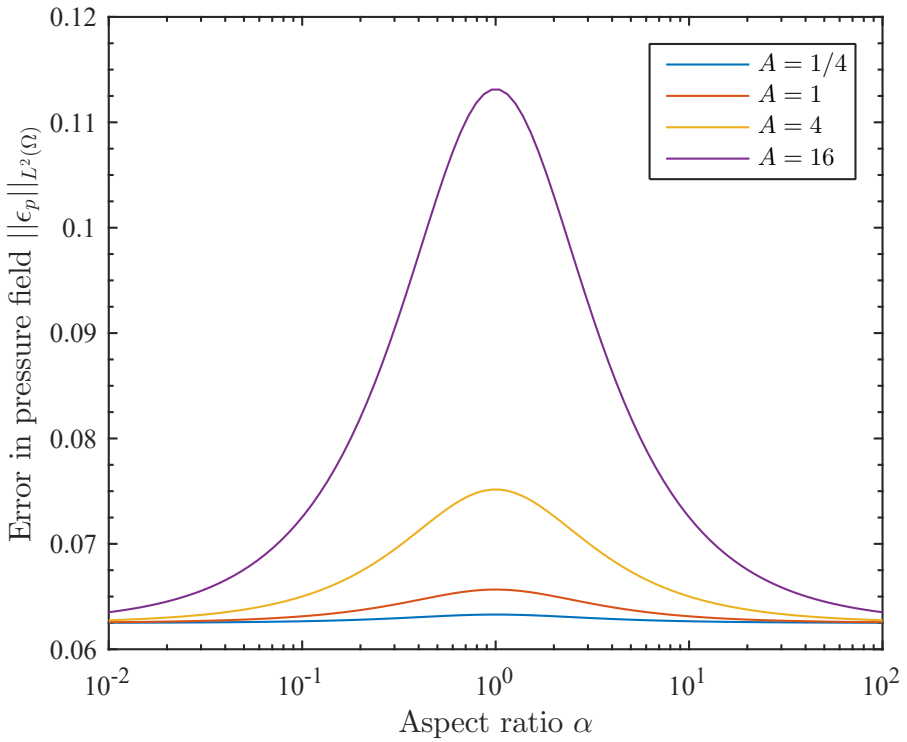

Figure 4.3: Error level in the pressure field versus aspect ratio of rectangular flow domains with various areas. The lines are plotted from inequality (4.14), with $|| \epsilon_f ||_{L^2(\Omega)} = || \epsilon_h ||_{L^\infty} = 2^{-4}$; and $A = 1/4, 1, 4, 16$, where the lines mark the upper bound of the inequality.

To compare the contributions of the uncertainty in the field and on the boundary, one can define a nondimesional number (R_{fb}) which is the ratio of the coefficient of the errors in the field ($|| \epsilon_f ||_{L^2(\Omega)}$, inequality (4.14)) and on the boundary ($|| \epsilon_h ||_{L^\infty(\partial\Omega)}$, inequality (4.14)). For a 2D rectangular Dirichlet domain, R_{fb} reads

$$R_{fb} = \frac{\alpha A}{\pi^2(1+\alpha^2)}. \tag{4.15}$$

When $R_{fb} \ll 1$, the error on the boundary tends to dominate the error in the pressure field, with limited budget or experimental accessibility, the best way to reduce the error in the pressure field would be to improve the error on the boundary. As an example, for small areas when $A \sim 1$, then $R_{fb} \in (0, 1/2\pi^2] \ll 1$, this relatively narrow interval implies that for a domain with nearly unit area, most error in the pressure field is likely contributed by the error on the boundary, while changing

the aspect ratio will not significantly affect the error in the pressure. However, because $R_{fb} \sim A$, the contribution of the error in the flow field increases quickly with larger domain areas.

One more comment on the Dirichlet boundary condition is that the error in the pressure field is due to the L^∞ norm of the uncertainties on the boundary, which is the largest error on the boundary, rather than the average error level measured by the L^2 norm. It suggests that one sharp and high error peak on the boundary may significantly increase the error propagation in the pressure field. Thus, one should try to avoid outliers on the boundaries if Dirichlet boundary conditions are applied.

4.4.2 Neumann case

For a domain with Neumann boundary conditions, we can obtain the error in the pressure field using similar analyses to section 4.4.1. Here, a zero mean error of the data in the field ($\int \epsilon_g \, d\Omega = 0$; see A.2 for more details) is assumed, which is the compatibility condition of the Poisson equation with pure Neumann boundary conditions. The error in the pressure field can then be bounded as

$$|| \epsilon_p ||_{L^2(\Omega)} \leq C_N || \epsilon_f ||_{L^2(\Omega)} + \sqrt{C_N C_{NB}} || \epsilon_g ||_{L^2(\partial\Omega)}, \tag{4.16}$$

where C_N and C_{NB} are the Poincare constants for the Neumann domain and the Neumann boundary, respectively.

We now validate the bound introduced by inequality (4.16), similar to section 4.4.1, by considering a steady 2D potential vortex in an $L \times L$ domain. Inequality (4.16) becomes:

$$|| \epsilon_p ||_{L^2(\Omega)} \leq \frac{1}{\pi^2} || \epsilon_f ||_{L^2(\Omega)} L^2 + \frac{4}{\pi^{3/2}} || \epsilon_g ||_{L^2(\partial\Omega)} L. \tag{4.17}$$

We construct the same flow as in the Dirichlet case, of which the nondimensionalized velocity field is $u = -y, y \in (-L/2, L/2)$; $v = x, x \in (-L/2, L/2)$, where u and v are the two components of the velocity field $\boldsymbol{u}$ in the 2D Cartesian system. Thus, $f(\boldsymbol{u}) = -2$, and the pressure field is $p = (x^2 + y^2)/2$. To satisfy the compatibility condition of the Neumann boundary Poisson equation, the Neumann boundary conditions are $\nabla p \cdot \boldsymbol{n} = -1, x = y = -L/2$, and $\nabla p \cdot \boldsymbol{n} = 1, x = y = L/2$.

Similar to section 4.4.1, a constant artificial error is constructed: $\epsilon_f = 2^{-4}$, and $\epsilon_g = 2^{-4}$, the error level in the domain and on the boundary are constants ($|| \epsilon_f ||_{L^2(\Omega)} = || \epsilon_h ||_{L^\infty(\partial\Omega)} = 2^{-4}$).

Introducing the error to the field only, on the boundary only, and both in the field and on the boundary, simulations agree with the theoretical analyses (figure 4.4). Error in the pressure field scales as the square of the domain length ($\sim L^2$) for large scale flow fields; however, for smaller flow fields, error scales by the domain length ($\sim L$).

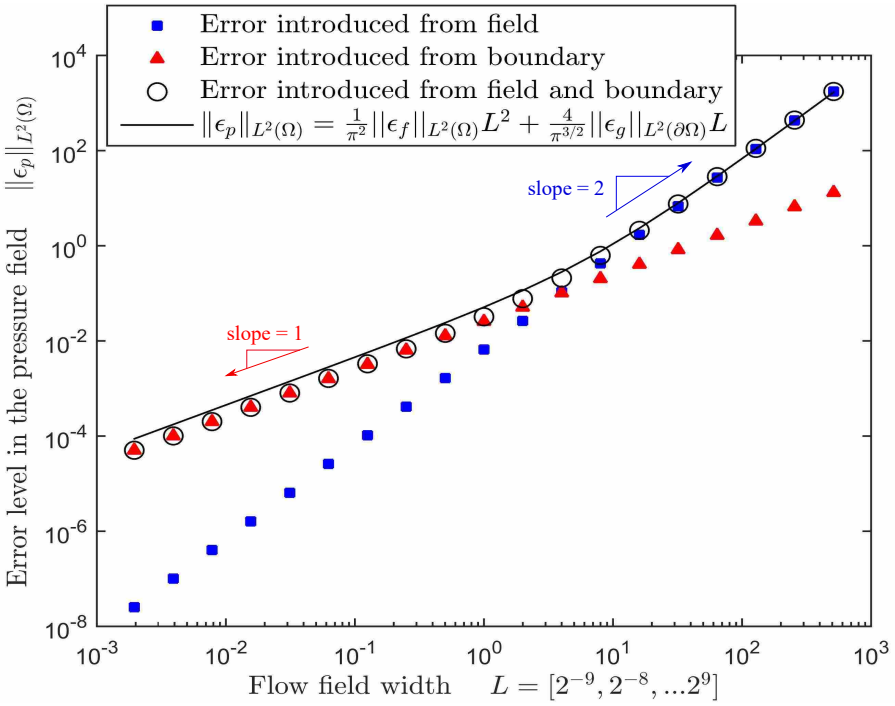

Figure 4.4: Error level in the pressure field versus the length scale of the flow field for the Neumann case. The data points illustrate the error level when artificial error is introduced in the field only (blue square), on the boundary only (red triangle), and in both field and on boundary (black open circle), respectively. The black solid line presents the bound of the error of the pressure field.

We also consider the more general case of a rectangle, 2D $N \times M$ field with area A, and aspect ratio α. Inequality (4.16) then becomes

$$|| \epsilon_p ||_{L^2(\Omega)} \leq \frac{1}{\pi^2} A \alpha^{\mathrm{sgn}(\alpha-1)} || \epsilon_f ||_{L^2(\Omega)} + \frac{2}{\pi^{3/2}} \sqrt{A}(\alpha^{\mathrm{sgn}(\alpha-1)} + 1) || \epsilon_g ||_{L^2(\partial\Omega)}, \tag{4.18}$$

Figure 4.5 shows an illustration of the error bound in the pressure field when the Neumann bounday conditions are applied. For a domain with fixed area, the square domain with $\alpha = 1$ leads to

minimum error propagation. However, when an elongated domain is used, the error in the pressure may not be bounded when $\alpha \to 0$ or ∞, because the error in the pressure field is dominated by the error on the longer boundaries. Thus, in engineering practice, a square domain is recommended for Neumann boundary conditions. If an elongated domain must be used, precise Neumann boundaries should be applied to the longer boundaries, or a smaller domain should be used to reduce the error accumulation.

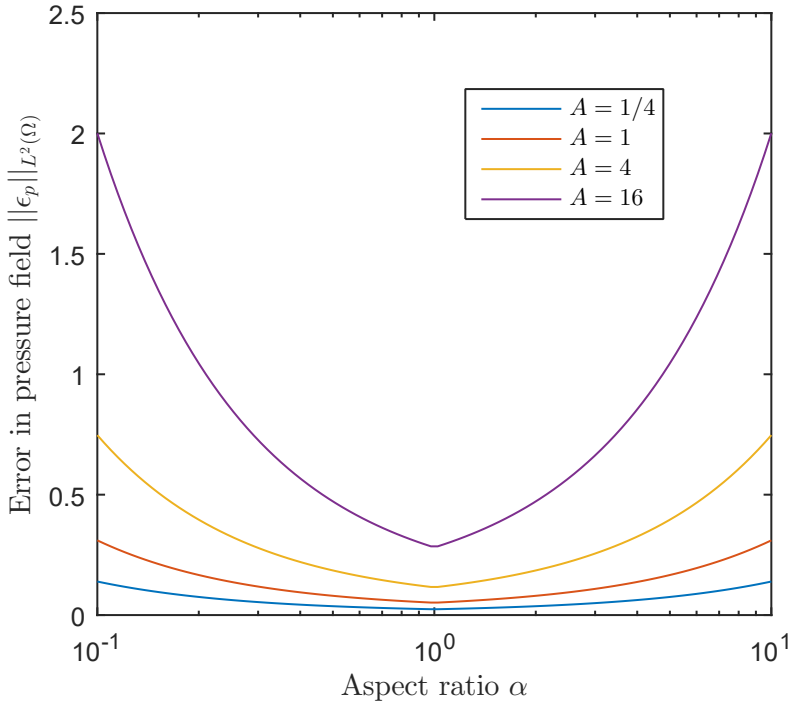

Figure 4.5: Error level in the pressure field versus aspect ratio of rectangular flow domains with various areas. The lines are plotted from equation 4.14, with $|| \epsilon_f ||_{L^2(\Omega)} = || \epsilon_h ||_{L^\infty} = 2^{-4}$; and $A = 1/4, 1, 4, 16$.

Similar to section 4.4.1 we compare the coefficients of inequality (4.18) and formulate the contribution ratio as

$$R_{fb} = \frac{\sqrt{\pi}}{2} \frac{\alpha^{\mathrm{sgn}(\alpha-1)}}{\alpha^{\mathrm{sgn}(\alpha-1)} + 1} \sqrt{A}. \tag{4.19}$$

A fixed domain area, for example $A \sim 1$, yields a relatively wide interval compared with the Dirichlet case ($R_{fb} \in [\sqrt{\pi}/4, 1)$). The implication is that the aspect ratio can be easily used to control the contribution from the field and boundary, depending on the specific practices of the experiments.

On the other hand, $R_{fb} \sim \sqrt{A}$, meaning that the contribution ratio is proportional to the length scale of the domain, and thus not as sensitive as Dirichlet boundary conditions to the scale of the domain.

The last comment on the pure Neumann boundary case is about the derivation of the error bound in the pressure field, and more details can be found in the appendix. The inequality (4.16) is obtained based on a weak or unrealistic assumption (i.e., the mean value of error in the data field is zero). Systematic error in the experiments is not necessarily a mean zero field (e.g., Gaussian errors). This could conflict with the compatibility condition and eventually render the Poisson solver intractable. Once the compatibility condition is not satisfied by the data, the solution to the Poisson equation does not even exist. One can usually get some results (we would rather not call them solutions) from a numerical Poisson solver even if the compatibility condition is not satisfied, however, the results highly depend on the numerical scheme, resolution, and convergence criteria of the numerical solver. Thus, pure Neumann boundary conditions should be avoided if possible, unless the PIV experiments have reasonably high accuracy, or the engineering application allows Neumann boundaries only. This tricky message is brought up by very few in the literature (e.g., Neeteson and Rival [43] mention this but don't explain why it happens). This may be the reason why most researchers use Dirichlet or mixed boundaries; although, technically, if one can use Dirichlet BCs, Neumann BCs are also an option. We did an exhaustive literature review for the related papers published in major journals and conferences in the last five years, and found that by default the community by and large utilized Dirichlet BCs whenever possible and shied away from Neumann BCs (see table 4.1). Two studies used pure Neumann BCs, however, they either have no accessibility to Dirichlet boundaries (e.g., internal flows of Löhrer et al. [44]), or a relatively small domain is used for an external flow without a confident far field assumption (e.g., Villegas et al. [45]).

Table 4.1: Types of boundary conditions used in recent studies

Type of BCs	Papers [a]
Dirichlet BCs	Neeteson and Rival [43] [b];
Neumann BCs	Löhrer et al. [44], Villegas et al. [45];
	Jalalisendi et al. [46], Oren et al. [35], Lignarolo et al. [24];
	de Kat et al. [47], Novara and Scarano [48], Pröbsting et al. [49];
Mixed BCs	Albrecht et al. [50], Nila et al. [27], Ghaemi and Scarano [51];
	Ghaemi et al. [52], Koschatzky et al. [53], Moore et al. [28];
	Violato et al. [54], and many more [c]

[a] We only count the papers that utilize the pressure Poisson approach.

[b] This paper tested both Dirichlet and Neumann boundaries for comparison.

[c] We apologize that we cannot list the many more informative papers that used mixed boundary conditions, but we cannot have all of them listed in this table.

4.4.3 Mixed boundary conditions

We see complicated and distinctly different error propagation dynamics simply from the boundary conditions even for these simple 2D domains. However, in engineering practice, mixed boundary conditions are more common due to the limitations and/or applications of the experiments (table 4.1). We now focus on the coupled dynamics of how the geometry and boundary conditions impact the error propagation in more complicated situations (e.g., a rectangular domain with two Dirichlet boundaries, and two Neumann boundary conditions on the opposite edges of the domain, respectively).

Consider a flow in a 2D rectangular domain ($N \times M$), with mixed boundary condition ($p = h$, $y = \pm N/2$; and $\nabla p \cdot \boldsymbol{n} = g$, $x = \pm M/2$). This physically means that the aspect ratio can be viewed as the relative amount of the boundary dictated by a Neumann condition to that given by a Dirichlet condition. The mixed boundary condition case can be decomposed into three parts, one that incorporates the error in the bulk of the domain, one for the error on the Neumann part of the boundary, and a third that accounts for the error on the Dirichlet part of the boundary. The analysis of the the error from the boundary terms is inherently difficult to estimate. However,

for a sufficiently large convex domain one would expect the error in the interior of the domain to dominate the boundary error, and the analysis of the contribution of the error from the field is already enough to lend itself rich physical insight. We again estimate the error in the pressure field using our previous analysis:

$$|| \epsilon ||_{L^2(\Omega)} \lesssim \frac{A\alpha}{\pi^2} || \epsilon_f ||_{L^2(\Omega)}. \tag{4.20}$$

The inequality is plotted in figure 4.6 and shows that for a domain with constant area a larger aspect ratio (i.e., more influence from Neumann boundaries) results in large error propagation with a trend that is as fast as the pure Neumann case. This implies that if a mixed boundary condition is utilized in a rectangular domain, Dirichlet conditions should be used on the longer sides of the boundary to mitigate the error propagation.

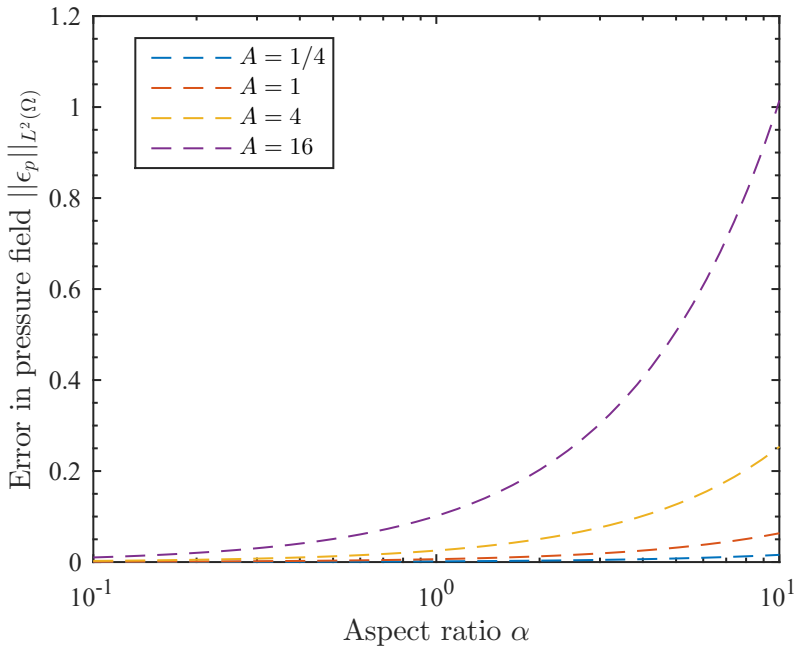

Figure 4.6: Error level in the pressure field versus aspect ratio of rectangular flow domains with various areas. The lines are plotted from inequality (4.20), with $|| \epsilon_f ||_{L^2(\Omega)} = 2^{-4}$; and $A = 1/4, 1, 4, 16$.

4.5 Discussion

We have shown that the upper bound of the error in the pressure field is related to the type of boundary conditions, geometry and the scale of the flow domain. The results include the explicit dependence on the geometry (the shape and boundary of the domain is incorporated in the Poincare constant), dimension (2D or 3D), and numerical scheme of the Poisson solver. One can use these results to design and minimize the error in an experiment before it is performed. For example, one can adjust the aspect ratio, area of the domain, and the type of boundary conditions to reduce the error propagation from the velocity field to the pressure field based on the reasoning outlined in section 3.4.

We can illustrate how one might use this information by using a simple example to present how to choose boundary conditions. Assume a square domain is used in a PIV experiment and the error level in the data and on the boundary is given and plotted in figure 4.7. We introduce the same error to the data in the field and the boundary for the pure Dirichlet and pure Neumann cases ($|| \epsilon_f ||_{L^2(\Omega)} = 2^{-3}$, $|| \epsilon_h ||_{L^2(\partial\Omega)} = || \epsilon_g ||_{L^2(\partial\Omega)} = 2^{-3}$), and compare them to cases where the error on the boundary is smaller ($|| \epsilon_f ||_{L^2(\Omega)} = 2^{-3}$, $|| \epsilon_h ||_{L^2(\partial\Omega)} = || \epsilon_g ||_{L^2(\partial\Omega)} = 2^{-4}$) as shown in figure 4.7 to illustrate the effect of lowering the error on the boundaries for both pure cases. We can now use figure 4.7 to illustrate how to choose boundary conditions when both Neumann and Dirichlet BCs are accessible. When the domain is large (e.g., $L > 10$) and the error on the boundaries is large ($|| \epsilon_h ||_{L^2(\partial\Omega)} = || \epsilon_g ||_{L^2(\partial\Omega)} = 2^{-3}$, solid lines in figure 4.7), the Neumann boundary conditions yield about twice the error of the Dirichlet boundary. Thus, choosing Dirichlet boundary conditions is best when the the domain is large. However, when the domain is small (e.g., $L < 10$), the Neumann BCs yield smaller error. If Neumann BCs are the only choice, one can either improve the experiments with more accurate boundary conditions (e.g., green dashed line, $L < 3.8$, comparing with the red solid line), or use a smaller domain (e.g., blue solid line, $L < 1.3$). However, in practice, the scale of the non-dimensionalized flow field is usually large ($L > 1$), thus the best choice is accurate Dirichlet BCs with a small flow domain (purple dashed line). Even for these very simple cases it is complicated to choose the proper BC settings, thus we suggest that users plot their own figure like figure 4.7 to design/optimize their own experiments. A detailed users guide is beyond the scope of this chapter and we will give more discussion in the next chapters.

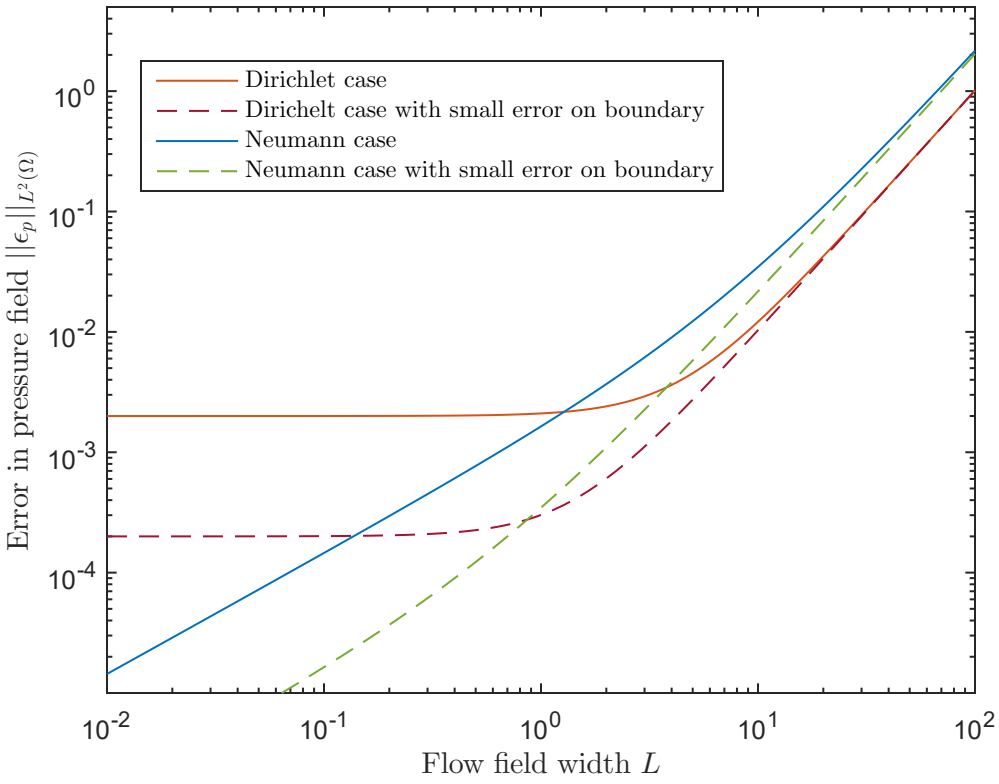

Figure 4.7: Bounds of the L^2-norm of error in a pressure field. The red and blue curves indicate the highest possible uncertainty level in the pressure field with the same level of error introduced in the data (2^{-3} on boundary and in field) for Dirichlet and Neumann cases, respectively. The purple and green dashed lines show Dirichlet and Neumann case with the same uncertainty level as other cases in the flow field, but with less error (2^{-4}) on the boundaries.

In this dissertation, we limited the discussion of the error propagation from the data to the pressure field (denoting as $||f(\boldsymbol{u})|| \rightarrow ||p||$), but the error propagation from the velocity field to the data (denoting as $||\boldsymbol{u}|| \rightarrow ||f(\boldsymbol{u})||$) was not covered. To bound $||f(\boldsymbol{u})||$ with $||\boldsymbol{u}||$ is not an easy task due to the nonlinear terms in the Navier-Stokes equation (e.g., $\boldsymbol{u} \cdot \nabla \boldsymbol{u}$) making the 2D solution inherently complicated. The 3D version of the propagation of error from the velocity field to the data is related to the well-posedness of the 3D Navier-Stokes equation, which is a Millennium Prize Problem. For this reason we do not expect to make significant progress in this area, at least in 3D.

Instead of a full solution to $||\boldsymbol{u}|| \rightarrow ||f(\boldsymbol{u})||$, we can attempt to calculate the error propagation from the velocity vector field to the data field. These first steps of calculation can provide

qualitative intuition of the error propagation in the whole pressure calculation process:

$$\epsilon_f = f(\boldsymbol{u} + \boldsymbol{\epsilon_u}) - f(\boldsymbol{u}), \tag{4.21}$$

where $\boldsymbol{\epsilon}_u$ is the error vector in the velocity field. Depending on the dimension and non-dimensional numbers in the Navier-Stokes equations (e.g., Reynolds number Re, etc.), equation (4.21) can be very long, however, the 2D convection term alone should be enough to illustrate the physics. Assuming that ϵ_u is sufficiently small, we can neglect the second order terms in the error (e.i., $(\partial\ \epsilon_u\ /\partial x)^2$, and $(\partial\ \epsilon_v\ /\partial y)^2$) to approximate (4.21) as:

$$\epsilon_f \approx -2\left(\frac{\partial u}{\partial x}\frac{\partial\ \epsilon_u}{\partial x} + \frac{\partial v}{\partial x}\frac{\partial\ \epsilon_u}{\partial y} + \frac{\partial u}{\partial y}\frac{\partial\ \epsilon_v}{\partial x} + \frac{\partial v}{\partial y}\frac{\partial\ \epsilon_v}{\partial y}\right), \tag{4.22}$$

where u and v are the velocity components, and ϵ_u and ϵ_v are the velocity error in the x and y direction, respectively. Recalling that $\|\ \epsilon_f\ \|_{L^2(\Omega)}$ is the source of the error from the velocity field that appears as data in the pressure field calculation (e.g., inequalitites (4.12) and (4.16)), $||\ \epsilon_f\ ||_{L^2(\Omega)}$ is calculated by integrating ϵ_f^2 over the whole domain. Utilizing the Cauchy-Schwarz inequality and applying index notation to (4.22) we arrive at

$$\|\ \epsilon_f\ \|_{L^2(\Omega)} \leq 2\left\|\frac{\partial u_i}{\partial x_j}\right\|_{L^2(\Omega)}\left\|\frac{\partial\ \epsilon_j}{\partial x_i}\right\|_{L^2(\Omega)}. \tag{4.23}$$

Noticing that the first term, $\left\|\partial u_i/\partial x_j\right\|_{L^2(\Omega)}$, in (4.23) is actually the gradient of the velocity field, we are be able to obtain some qualitative sense of the reason why the type of the flow affects the error propagation. Physically this means that the velocity gradient directly influences the error level, so for spatially accelerating flow fields the error will inherently be larger. This preliminary discussion is supported by experimental results and physical intuition outlined by Charonko [3].

We have intentionally made the results of this work unrelated to any specific numerical scheme. The error bound derived here may be saturated by the worst case scenario with the best numerical implementation. This means that if we solve the pressure equation perfectly with an exact numerical scheme, given a certain level of error in the velocity field, the error in the pressure field will be below the error bound. On the other hand, the numerical error is not considered

here, and one may expect larger error than the bounds if the numerical solver is not implemented properly.

One more note on the the non-dimensionalization of the problem may help with practical implementation. The characteristic length scale of the flow field is exactly the characteristic length (L_0)) of the Reynolds number, $Re = \rho \boldsymbol{u} L^*/\mu$, where ρ and μ are the density and viscosity of the fluid. The pressure can also be related to the characteristic length scale through the non-dimensionalization. For instance, the pressure or error in the pressure can be non-dimensionalized by either a dynamic pressure ($P_0 = 1/\rho U_0^2$, useful for large Re flows), or by a length scale and viscous stresses ($P_0 = L_0/\mu U_0$, useful for viscous flows), where U_0 is the characteristic velocity of the flow. Thus, the predicted absolute error in the pressure field with real units should be $E_p = || \epsilon_p ||_{L^2(\Omega)} P_0$. If we define relative error as $E_p/P_0 \times 100\%$, we will see that $|| \epsilon_p ||_{L^2(\Omega)}$ actually has physical meaning as a measurement of the relative error of the pressure field. Finally, it isn't necessary to work with the non-dimensionalized Navier-Stokes equation and the pressure Poisson equation as we did here, rather one could re-derive these error bounds dimensionally, but the conclusions would remain the same yet be more difficult to interpret.

At last, under the framework proposed in this work, we try to connect two popular categories of methods for PIV-based pressure field calculation: i) pressure Poisson equation based methods, which work with Laplacian of the pressure field derived by applying divergence on a rearranged Navier-Stokes equation (e.g., de Kat and van Odheusden [21]); and ii) Navier-Stokes equation based methods, which directly integrate the pressure gradient in the Navier-Stokes equation (e.g., Dabiri et al. [4], as well as Liu and Katz [32]). One may notice that the derivation from the incompressible Navier-Stokes equation to (4.1) according to the statement of the problem is not based on any additional assumptions. This implies that the analysis and the results of the pressure Poisson equation (4.1) in this dissertation should hold for the Navier-Stokes equation based methods too. For example, a large domain accumulates more error in the pressure field from inaccurate velocity measurement, and Dirichlet BCs tends to yield less error than Neumann BCs, etc. The rigorous validation of this point is beyond the scope of this dissertation research, and we sincerely welcome discussion and collaboration on this topic in future studies.

4.6 Summaries

In this chapter, we have analyzed the error propagation dynamics inherent in the calculation of the pressure Poisson equation from velocity data common to many PIV experiments. We emphasize that this work sets up a framework for analyzing the power/level of the error in the pressure field. The framework is based on a natural idea that the error in the pressure estimation is a combination of the true value and the error; and the measure of this error can be well defined with the L^2 & L^∞ norm. Under this framework, we directly analyze the error in the data as non-negligible perturbations to the pressure Poison equation, and have been able to unravel the dynamics that affect error propagation, namely: the shape, area/volume, and boundary conditions of the flow domain.

This work lays out guidelines for designing experiments (velocity field measurements) that can be used to calculate the pressure field via the pressure Poisson equation. In engineering practice, the techniques presented can be used to develop *a priori* error estimations of the pressure field to inform the practical side of experiments and minimize the error propagation inherent in calculating pressure fields from velocity fields.

CHAPTER 5. USERS' GUIDE: ONE SIMPLE EXAMPLE

5.1 Introduction

In Chapter 4, the error bounds are derived based on the non-dimensional Navier Stokes equation, thus all the results are also non-dimensional (e.g. inequalities (4.12) and (4.16) et al.). Examples in this chapter will illustrate how to use the results in chapter 4 to design and optimize an experimental data collection. Again, a synthetic flow that has an exact solution for both the velocity and pressure field as a benchmark is used. These calculations are dimensional and units to improve insight into the actual application. This section can also be considered a further validation of chapter 4 and an introduction to some open problems (see chapter 7) that will be addressed hereafter.

5.2 Synthetic experiments and artificial error

5.2.1 Design of experiments

Consider experimentalist Mrs. Randi H. Pan who is aiming to study the transition and decay in a Taylor-Green vortex array. Although this is difficult and expensive in practice, it is assumed that Randi was successful in creating a two-dimensional Taylor-Green vortex array with water in a pool.

The target of Randi's experimental research is to investigate the interaction and development of a Taylor-Green vortex, similar to the research of Brachet et al. [55]. Time resolved 2D PIV and PIV based pressure calculations will be used to observe the physics of the vortex array. The first step of this research is to use a steady state inviscid flow to validate the experimental setup. Based on her research goals, Randi has some *preferences* regarding the experiments, which are listed below:

P-i) At least two vortex cells, or vortex centers, and one boundary between cells should be visible in a single frame to investigate the interaction between the cells;

P-ii) The more vortex cells covered in one PIV domain the better;

P-iii) The size of the vortex cells will preferably be on the order of 0.5 m.

However, due to the financial and physical restrictions of Randi's experimental setup, she has some *limitations*:

L-i) Resolution of the 2D PIV cannot be higher than 512×512 per $1\,\mathrm{m} \times 1\,\mathrm{m}$ domain;

L-ii) The water pool is square, and the length of the edge cannot be larger than 5 m. Because the wall effect should be avoided, a $5\,\mathrm{m} \times 5\,\mathrm{m}$ pool is barely enough to set up a small vortex array (e.g. $2\,\mathrm{m} \times 2\,\mathrm{m}$) in the center of the pool.

Based on the conclusions of chapter 4, some basic *rules* should be followed to minimize the error propagation from the velocity field to the pressure field, which are listed below:

R-i) Small domains should be used to reduce error propagation;

R-ii) Pure Neumann boundary conditions should be avoided if possible;

R-iii) If Neumann boundary conditions are used, a square domain (aspect ratio $\alpha = 1$) is recommended;

R-iv) Large velocity gradients should be avoided in the domain and on the boundary if possible;

Comprehensive consideration of the listed research *preferences*, experimental *limitations*, and *rules* introduced in chapter 4 leads to preliminary experimental *design* profiles as shown in figure 5.2 (more mathematical details can be found in section 5.2.2). The flow of the preliminary design process is shown in figure 5.1 and Randi's pathway is highlighted by the green arrows. The figure also provides a convenient graphical representation guide for future user.

D-i) Bernoulli's principle, or far field assumptions, do not apply in the vortex array, thus Neumann boundary conditions have to be applied;

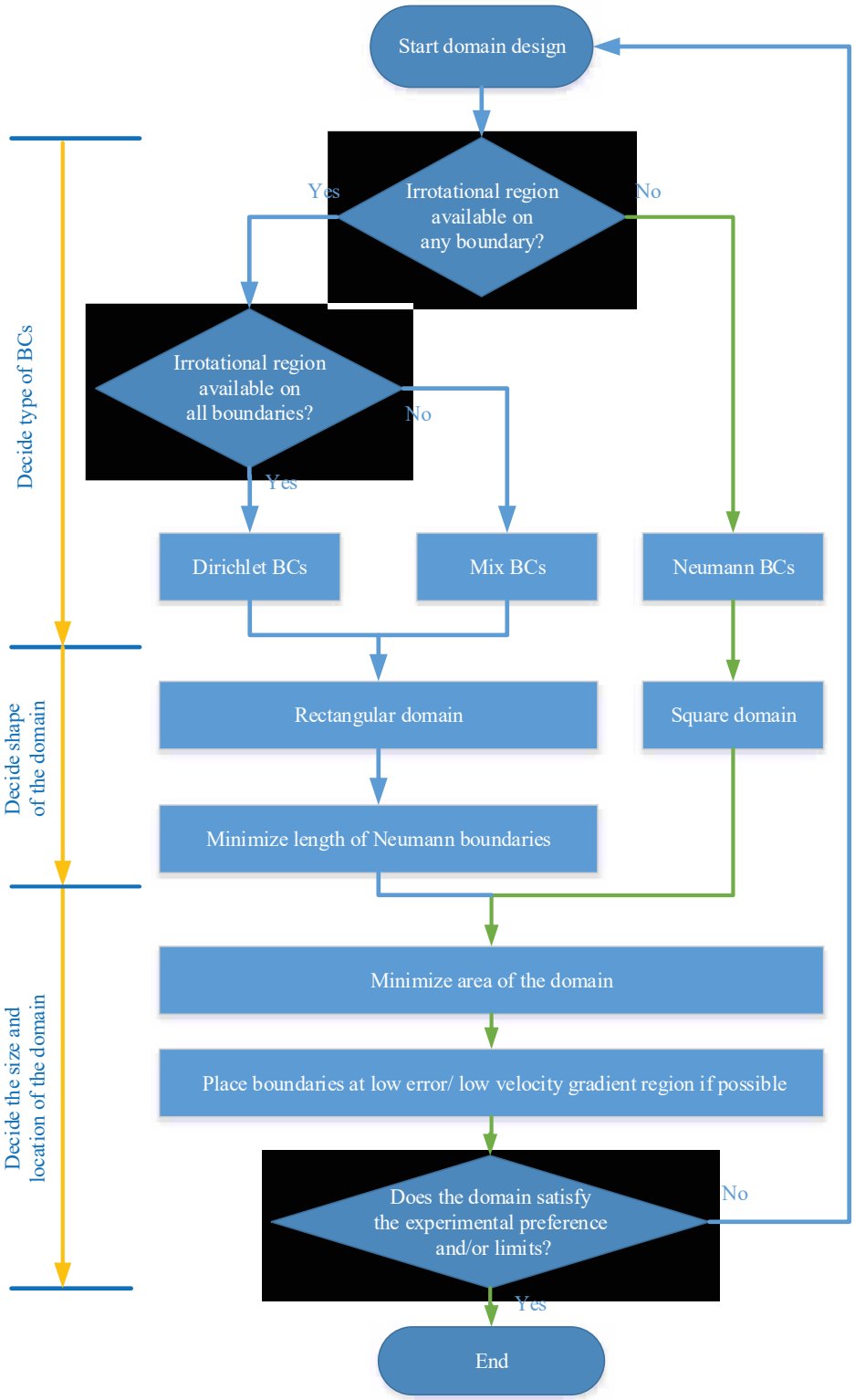

Figure 5.1: Flow chart of a typical experimental design process. The orange arrows highlight the stages of the experimental design. The green pathway highlights the design flow of Randi's preliminary experimental design. The theoretical basis of this flow chart can be found in Chapter 4.

D-ii) According to the analysis in chapter 4 (e.g. inequalities 4.16), the smallest square domain that covers more than one vortex cells is a domain that can cover 2×2 cells. It is expected that this domain yields the least error propagation;

D-iii) The boundary of the domain will be placed at an area where the velocity gradient is small (e.g. the boundaries of the domain overlap the boundary of the cells).

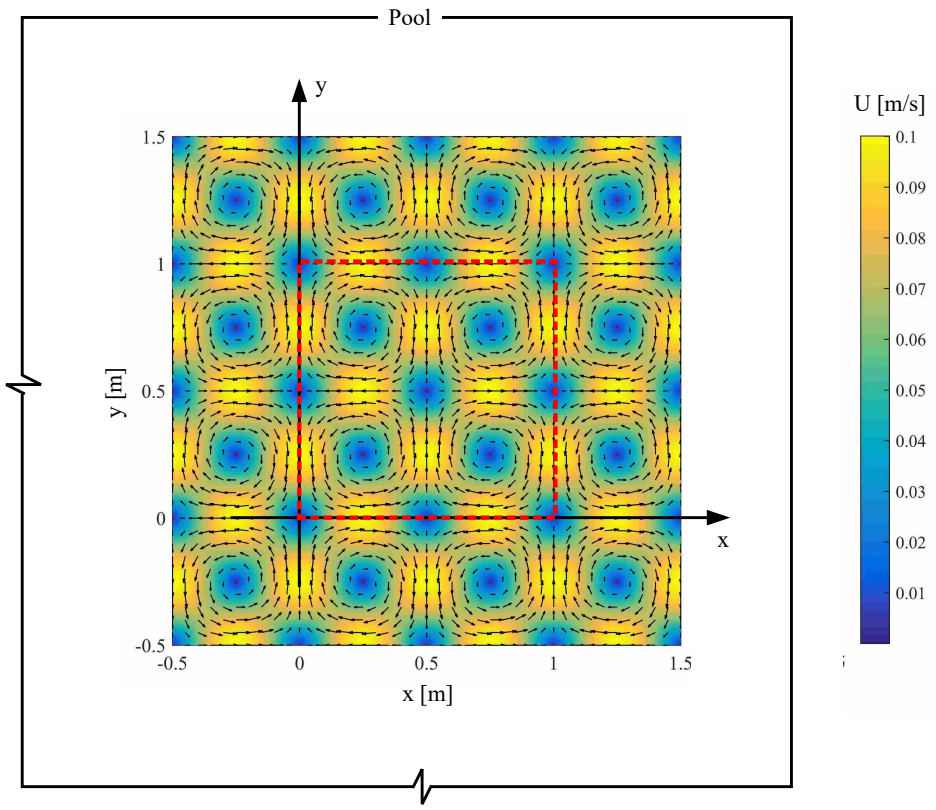

Figure 5.2: Preliminary experimental design. The quiver plot over the amplitude of the velocity shows the flow field in the center of the water pool. The flow in the red dashed box is the domain that will be used for PIV-based pressure calculation.

For this steady-state laminar flow, the characteristic length ($L_0 = 0.5\,\mathrm{m}$) that makes the most physical sense is the length scale of a vortex cell. Thus the the non-dimensional geometry of the domain is indeed a 2×2 square with Neumann boundary conditions, which corresponds to a $1\,\mathrm{m} \times 1\,\mathrm{m}$) domain (the red dashed box in figure 5.2). Thus inequality 4.17 gives the error bound

in the pressure calculation:

$$|| \epsilon_p ||_{L^2(\Omega)} \leq \frac{4}{\pi^2} || \epsilon_f ||_{L^2(\Omega)} + \frac{8}{\pi^{3/2}} || \epsilon_g ||_{L^2(\partial\Omega)}. \tag{5.1}$$

It is worth mentioning again that $|| \epsilon_f ||_{L^2(\Omega)}$ and $|| \epsilon_g ||_{L^2(\Omega)}$ are the error level of the data (not the velocity field) in the field and on the boundary, respectively. These two terms are not easy to evaluate. However, the specific value of these terms do not affect the experimental design, because the error distribution in the PIV results are indeed *priori* information, and thus unknown. In other words, it's fair to assume one already gets the best he/she can get in terms of experiments (e.g. particle density, interrogation window choice of PIV, etc.), and cannot do much to improve the PIV quality. Then, the design summarized by D-i) to D-iii) should give the best result.

However, Randi is not sure that the experimental design described above is the best choice. Fortunately, by using a synthetic Taylor-Green vortex flow, it is not difficult to examine this hypothesis.

5.2.2 Synthetic flow and artificial error

The 2D Taylor-Green vortex array has exact solutions. The velocity field reads

$$\begin{aligned} u &= U_0 \sin\left(\pi \frac{x}{L_0}\right) \cos\left(\pi \frac{y}{L_0}\right) \\ v &= -U_0 \cos\left(\pi \frac{x}{L_0}\right) \sin\left(\pi \frac{y}{L_0}\right), \end{aligned} \tag{5.2}$$

where $L_0 = 0.5\,\mathrm{m}$ is the wave length of the vortex array, and $U_0 = 0.1\,\mathrm{m/s}$ is the maximum velocity in the flow field. The pressure distribution reads

$$p = \frac{\rho U_0^2}{2} \cos\left(\pi \frac{x+y}{L_0}\right) \cos\left(\pi \frac{x-y}{L_0}\right), \tag{5.3}$$

where $\rho = 1 \times 10^3\,\mathrm{kg/m^3}$ is the density of water.

$L_0 = 0.5\,\mathrm{m}$ is chosen as the characteristic length of the flow, which is an inherent physical property of the flow. More explicitly, it is the length scale of the vortex cells. The kinetic pressure $P_0 = \rho U_0^2/2$ is chosen as the characteristic pressure since the Reynolds number is large ($Re =$

5.0×10^4 when $U_0 = 0.1\,\mathrm{m/s}$ is chosen as the characteristic velocity, and the viscosity of water is $1.0 \times 10^{-3}\,\mathrm{Pa \cdot s}$). With $u^* = u/U_0$, $\boldsymbol{x}^* = \boldsymbol{x}/L_0$, and $p^* = p/P_0$, and by dropping the superscript (*), the non-dimensionalized governing equations with respect to the velocity field are described as

$$\begin{aligned} u &= \sin(\pi x)\cos(\pi y) \\ v &= -\cos(\pi x)\sin(\pi y), \end{aligned} \tag{5.4}$$

and pressure field

$$p = \cos[\pi(x+y)]\cos[\pi(x-y)]. \tag{5.5}$$

The quantities of the synthetic flow are summarized in table 5.1.

Table 5.1: Values and dimensions of the variables used in the Green-Taylor vortex flow.

	Char. Len.	Char. Velo.	Char. Press.	Viscosity	Density	Re #
Notation	L_0	U_0	P_0	μ	ρ	Re
Value	0.5	0.1	5	1×10^{-3}	1×10^3	5×10^4
Dimension [a]	$[L]$	$[L][T]^{-1}$	$[M][L]^{-1}[T]^{-2}$	$[M][T]^{-1}[T]^{-1}$	$[M][L]^{-3}$	–

[a] SI unites are applied to all the dimensions.

To model the potential error introduced by the PIV experiments in a more realistic way, two types of error are added to the velocity field (but not the data field). i) systematic error:

$$\epsilon_{\boldsymbol{u}_1} = \epsilon_1\, \boldsymbol{u}, \tag{5.6}$$

where ϵ is a small constant. $\epsilon_{\boldsymbol{u}_1}$ will thus lead to the velocity components amplified by $100(1+\epsilon_1)\%$, which can be considered as error introduced by inaccurate calibration. ii) random error

$$\epsilon_{\boldsymbol{u}_2} = \epsilon_2\, \mathrm{Uni}(-1,1)\boldsymbol{n}, \tag{5.7}$$

where ϵ_2 is a constant, and $\mathrm{Uni}(-1,1)$ denotes variables that have a uniform distribution in $[-1,1]$, and $\epsilon_{\boldsymbol{u}_2}$ leads to a simple model of random error in the PIV results.

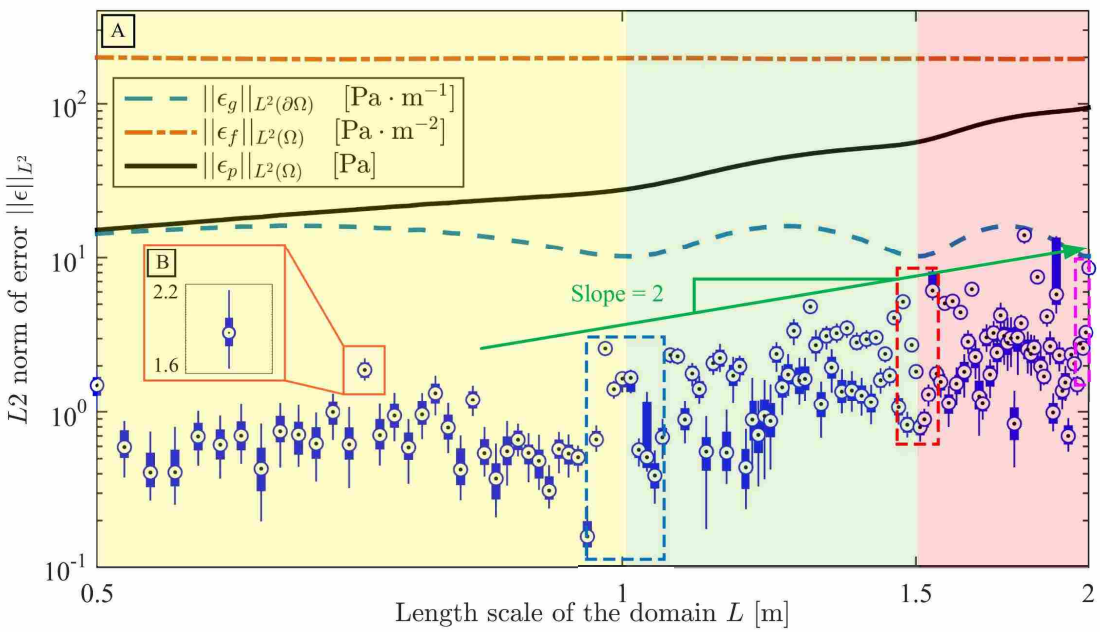

Figure 5.3: A). Error versus the length scale of the domain. The box plot indicates the error in a calculated pressure field with a synthetic velocity field (5.2), but contaminated by artificial error (5.6 and 5.7). The upper and lower edges of the solid blue boxes indicate 25$^{\text{th}}$ and 75$^{\text{th}}$ percentile, respectively. The target-like symbol ($\odot$) on each box indicates the median of the data. The error in the pressure field has units of [Pa]. The orange dash-dot line shows the error level in the field ($|| \epsilon_f ||_{L^2(\Omega)}$). The blue dashed line is the error on the boundary $|| \epsilon_g ||_{L^2(\partial\Omega)}$. The black solid line is the error bound calculated based on inequality (5.1). Units of the variables are shown in the legend. B). Zoomed-in view of one error box.

5.2.3 Validation of experimental design

Let ϵ_1 and ϵ_2 be small constants (for example, $\epsilon_1 = 2 \times 10^{-2}$ and $\epsilon_2 = 2\sqrt{3} \times 10^{-3}$)[1], and introduce these errors in the velocity field (equation 5.2). Figure 5.3 examines how the length scale of the domain affects error propagation.

In figure 5.3 A, the orange dash-dot line is the calculated error level inside the domain ($|| \epsilon_f ||_{L^2(\Omega)}$) by comparing the synthetic flow with and without artificial error introduced in the velocity field; similarly, the blue dashed line is the calculated error on the boundary of the domain ($|| \epsilon_g ||_{L^2(\partial\Omega)}$). With these two calculated errors ($|| \epsilon_g ||_{L^2(\partial\Omega)}$ and $|| \epsilon_f ||_{L^2(\Omega)}$) Randi calculated the error bound based on inequality (4.16), or more specifically, (5.1). The box-plot shows the error in the pressure field calculated with an artificial error contaminated velocity field. Each box

[1] ϵ_1 and ϵ_2 are chosen so that $|| \epsilon_{\boldsymbol{u}_1} ||_{L^2(\Omega)} = || \epsilon_{\boldsymbol{u}_2} ||_{L^2(\Omega)} = 1 \times 10^{-3}$. This choice of constants gives a measure of the error in the velocity components and forces them to have the same power level.

contains 100 data points (from 100 simulations). The open dashed blue, red and magenta boxes contains 10, 10 and 5 boxes around $L = 1, 1.5, \&2$ respectively. It is shown that all the boxes in the box-plot are all lower than the black solid line, and this implies that the error in the calculated pressure field is strictly bounded by the the theoretical error bound, as expected. The envelope of the box-plot follows the trend of the error bound fairly well, for example the top of the open dashed boxes generally follows a line with slope $= 2$ (see the green arrow in figure 5.3 A), which is also expected by the theoretical bound (black line). Note that in this case error level in the field is about 10 times larger than the error level on the boundary ($|| \epsilon_f ||_{L^2(\Omega)} \sim ||10\ \epsilon_g ||_{L^2(\Omega)}$), for a domain with length scale $L \in [1,2]$, although not typically big, the error in the flow field already dominates the error propagation, and error in the pressure field should be proportional to the area of domain ($|| \epsilon_f ||_{L^2(\Omega)} \sim L^2$).

The yellow patch in figure 5.3 A indicates the experimental domain with the length of edges $L \in [0.5, 1)$, which covers more than 1×1 vortex cell, but less than 2×2 cells. Although this region generally yields the smallest error compared to the other two regions (indicated by the green and red patches) of interest, it is not sufficiently large to resolve the potential physics. The red patch region ($L > 1.5$) covers more than 3×3 vortex cells, which is nice for the large field of the observation, however, this may lead to the domain being too close to the wall of the pool, which may introduce large errors and disturb the structure of the vortex array. Also, the error propagation is inherently enhanced by the large area of the flow domain and long perimeter of the boundary. The green region ($L \in [1, 1.5]$) is a feasible region that the domain can cover 2×2 to 3×3 vortex cells, that satisfy Randi's experimental requirements; and the error in the pressure field is generally small. In the green region, the least error in the pressure field is achieved at around $L = 1$. This is indeed Randi's original design based on the principles indicated in chapter 4.

Figure 5.3 can be also considered as a further validation to the theory in chapter 4. The errors (box-plots) are smaller and follow the trend of the theoretical prediction (black solid line), which agrees with the main conclusions based on inequality (4.16).

One may notice that the height of the error boxes is quite varied, even for nearby data sets which have the same amount of artificial error in the field and on the boundary, and a similar domain length scale. This implies that the pressure calculation is sensitive to the boundary (at least

for the Neumann boundary case). This phenomenon can be explained intuitively by examining the boundary condition equation (4.3), similar to the analysis in section 4.5.

The error on the Neumann boundaries is described by

$$\epsilon_g = g(\boldsymbol{u} + \epsilon_{\boldsymbol{u}}) - g(\boldsymbol{u}), \tag{5.8}$$

where $\epsilon_{\boldsymbol{u}}$ is the error vector in the velocity field. Again, the 2D convection term is examined to illustrate the physics. Assuming that $\epsilon_{\boldsymbol{u}}$ is sufficiently small, we can neglect the small terms in the error (e.g., $\epsilon_u \, \partial \, \epsilon_u \, / \partial x$ and $\epsilon_v \, \partial \, \epsilon_u \, / \partial y$) to approximate equation (5.8). The x component of the error, for example, on the boundary is

$$\epsilon_g \approx -\left(\epsilon_u \frac{\partial \, \epsilon_u}{\partial x} + u \frac{\partial \, \epsilon_u}{\partial x} + \epsilon_v \frac{\partial u}{\partial y} + v \frac{\partial \, \epsilon_u}{\partial y} \right), \tag{5.9}$$

where u and v are the velocity components, and ϵ_u and ϵ_v are the velocity errors in the x and y direction, respectively. Utilizing the Cauchy-Schwarz inequality and applying index notation to (5.9), it becomes

$$\| \, \epsilon_g \, \|_{L^2(\partial\Omega),i} \leq \epsilon_j \left\| \frac{\partial u_i}{\partial x_j} \right\|_{L^2(\partial\Omega)} + u_j \left\| \frac{\partial \, \epsilon_i}{\partial x_j} \right\|_{L^2(\partial\Omega)}, \tag{5.10}$$

where $\| \, \epsilon_g \, \|_{L^2(\partial\Omega),i}$ is the component i ($i = 1, 2$) of the error on the boundary of the data field. Inequality (5.10) shows that the error of the data on the boundary is related to the velocity and velocity gradient, as well as the error and the gradient of the error, which is even more complicated than the case for the error inside the domain (4.23).

On the other hand, even for a fixed domain (constant error level in the velocity field, and constant length scale of the domain), the error level in the pressure field varies significantly. For example, figure 5.3 B provides a zoomed-in view of one data set that contains 100 simulations for a small domain ($L \approx 0.6$). The error in the calculated pressure varies from approximately 1.6 Pa to 2.2 Pa. Considering that the maximum pressure for this domain is roughly 5 Pa without introduced artificial error, the variation of the error in the calculated pressure is fairly large. Also, noticing that this large variation is from a uniformly distributed random error with the constant statistical parameters (i.e., distributed in $[-\epsilon_2, \epsilon_2]$ and thus mean zero and constant power), this implies

that a different profile of the error in velocity field leads to a different level of error in pressure calculation. This is expected, if one recalls the inequalities (4.23, and 4.23).

It is also worth mentioning that the theoretical error bound overestimates the error propagation in in this synthetic experiment. I have to admit that it is not as favorable as Randi expected, however, the error bound overestimation is expected from the physics point of view. The profile of the error in the data field affects error propagation, but some error fields are less powerful. A related result is addressed by De Kat and Van Oudheusden [21]. They discovered that the Poisson solver based pressure calculation behaves like a low pass filter for both a velocity field input and the error in the velocity field, meaning that low frequency error propagates to the pressure calculation more effectively. One may ask why and how the error profile or type matters for the error propagation dynamics, which can raise some open problems that will be discussed in chapter 7.

If the imaginary Mrs. Randi H. Pan is offended, I apologize.

CHAPTER 6. EXPERIMENTAL VALIDATION

6.1 Introduction

In this section, we present an experimental validation to the theory introduced in chapter 4. PIV experiments of an oscillating flow in a 2D diffuser by King and Smith [5] will be used as input data. Pressure calculations from the PIV results will be compared with the experimental pressure measurements of a similar fashion used by Charonko et al. [3].

6.2 Method

As a data source in this chapter we use an oscillating flow in a 2D diffuser with a diffuser angle of 30° opening from a 1.66 cm diameter to 6.70 cm and driven by eight speakers (USU Oscillating Flow Facility [56,57]). The oscillating flow has a frequency of $f = 8.5\,\text{Hz}$ and a Reynolds number of approximately $Re_\delta = 580$ based on maximum velocity and viscous penetration depth ($\delta = 8.3 \times 10^{-4}\,\text{m}$). Simultaneous pressure at six locations on the diffuser wall is obtained by pressure transducers (see figure 6.3 for three of them on the left wall). For more explicit details, refer to [5]. Phase averaged, 2D volume flow rates and pressure measurements at port 4 and 6 (P_4 and P_6) over time in a single period are shown in figure 6.1.

Due to the limitations of the current theoretical solution (see chapter 4) and Poisson solver, which only apply to 2D rectangular domains, the in-house Poisson pressure solver requires that the direction of the structured mesh grid be either orthogonal or parallel to the boundary of the domain. To apply the pressure Poisson solver to the PIV results, the original velocity vector field is rotated 15° counterclockwise around the origin in the original coordinate system (see figure 6.2), and re-meshed by 2D triangulation-based cubical interpolation (from the original coordinate to the rotated system).

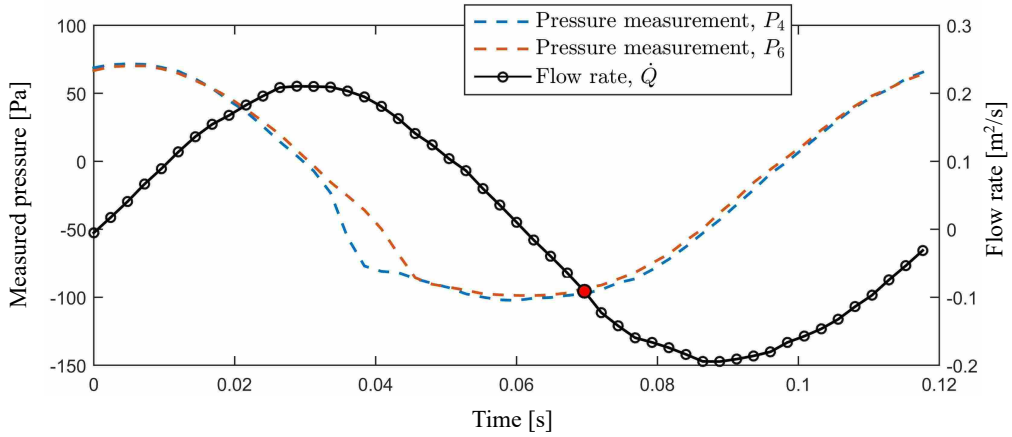

Figure 6.1: Phase averaged pressure measurement at P_4 and P_6 (dashed lines) and flow rate (black solid line with open marks) are plotted against time. The red circle denotes the frame shown in figure 6.3.

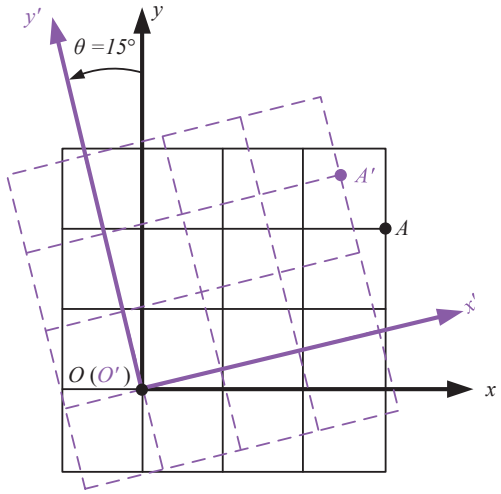

Figure 6.2: Coordinate transformation representation. The solid black coordinate frame corresponds to the original PIV data (see figure 6.3A for one frame of the real flow). The dashed purple coordinate systems is the result of the transformation (see figure 6.3B for one frame of the flow field after transformation).

After post-processing the original PIV data, three varying domains, with a single edge along the left wall of the diffuser, are used for validation (figure 6.3B, domain I is a $31.7\,\text{mm} \times 31.7\,\text{mm}$ square, domain II is a $45.0\,\text{mm} \times 45.0\,\text{mm}$ square, and domain III is a $31.7\,\text{mm} \times 63.5\,\text{mm}$ rectangle). Because the pressure measurements in the experiment are only available at three locations on the left side of the diffuser wall, the phase averaged pressure difference between pressure ports over one cycle is used as a benchmarking variable, rather than the $L2$ norm used previously. However, it is still expected that for the case of the Neumann boundary condition, a small square domain will produce the least error, even for this point-wise error measurement.

6.3 Results

Neumann boundary conditions are implemented on domains I, II and III to calculate the pressure fields. The pressure difference between P_4 and P_6 is used as a benchmarking to compare with the experimental results and pressure calculations, see figure 6.4. Pressure calculation in domain I (blue dashed line) generally follows the trend of the experimental result (purple line), although the error is typically large. Domain II gives a similar amount of error in the pressure calculation, but the trend is fallacious. Domain III leads to the largest error, with a result that differs significantly from the experimental data. Although these calculations are inaccurate, the performance is what is expected in terms of the error level in the pressure calculation; The pressure calculated from domain I yields more accurate results than domain II, which is more accurate than domain III. Based on the conclusions in chapter 4, one can easily derive the error bounds for each domain and see why domain I is the best choice and why domain III is the worst. Domain I has the smallest area and an aspect ratio of 1, while domain III has the same area as domain II (twice the area of domain I) but an aspect ratio 2. I would like to comment on the large error as shown in this simulation. First, if the pressure on the wall is influenced by the Stokes layer thickness, then ($\delta = 8.3 \times 10^{-4}\,\text{m}$) is the proper characteristic length, which leads to a non-dimensionalized area $A = 1.45 \times 10^3$ for domain I, and $A = 1.45 \times 10^3$ for domain II and III. Remember that the error in the velocity field from many different sources (e.g. calibration, random noise of PIV, out of plane vector, etc.) could lead to large error in the data. Specifically in the simulations contained in this research, coordinate transformations and interpolation introduce additional error, with the exact amount unknown yet non-negligible. For this reason, the error level in the data $|| \epsilon_f ||_{L^2(\Omega)}$ and

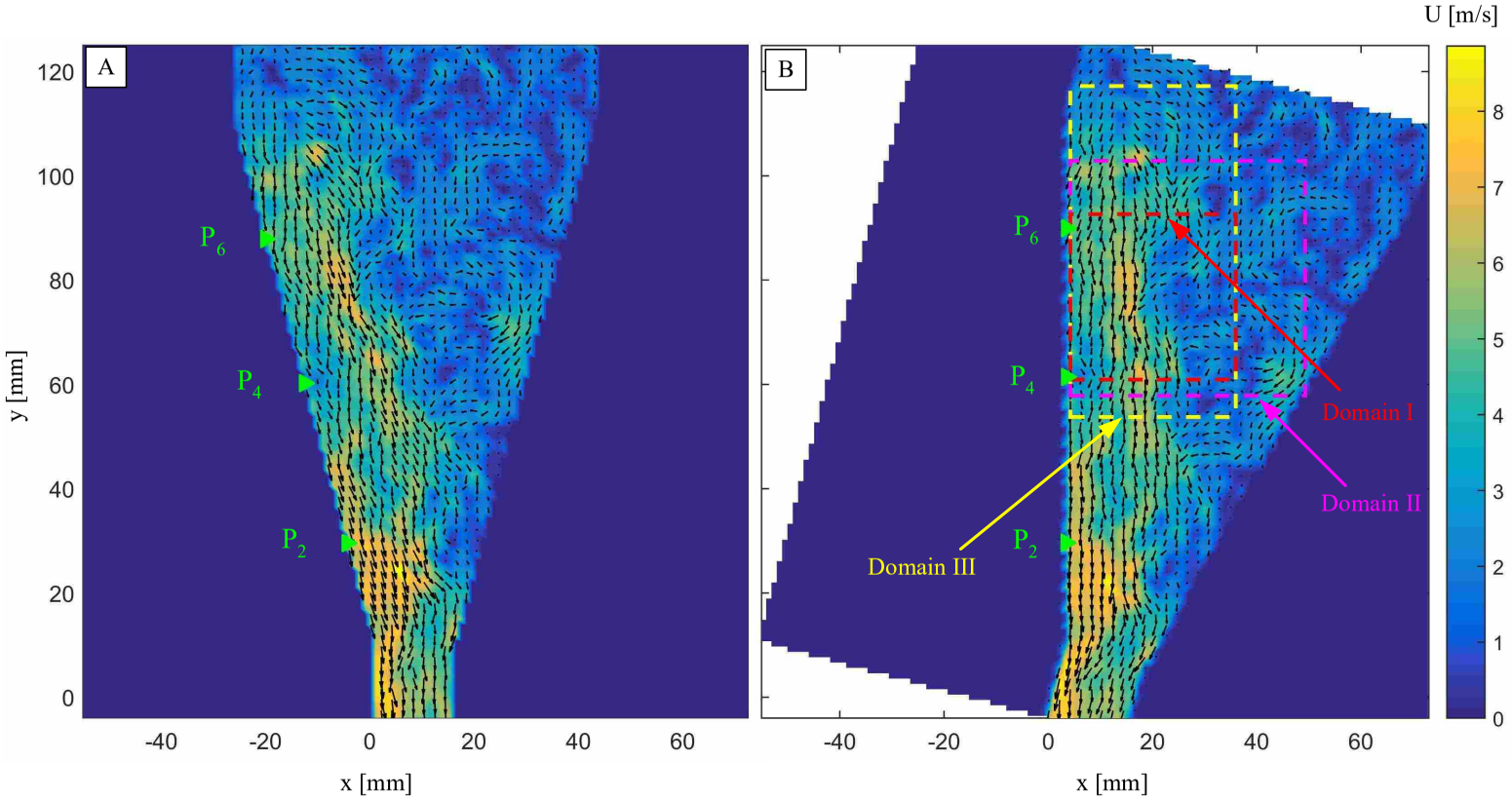

Figure 6.3: A). One frame of the flow field within the diffuser, presented by quiver plot over the velocity field. Three pressure ports (P_2, P_4, and P_6) are marked by green triangles. B). The same flow field rotated 15° in a counterclockwise direction. Three benchmarking domains (I, II and III) are marked with red, yellow, and magenta dashed boxes.

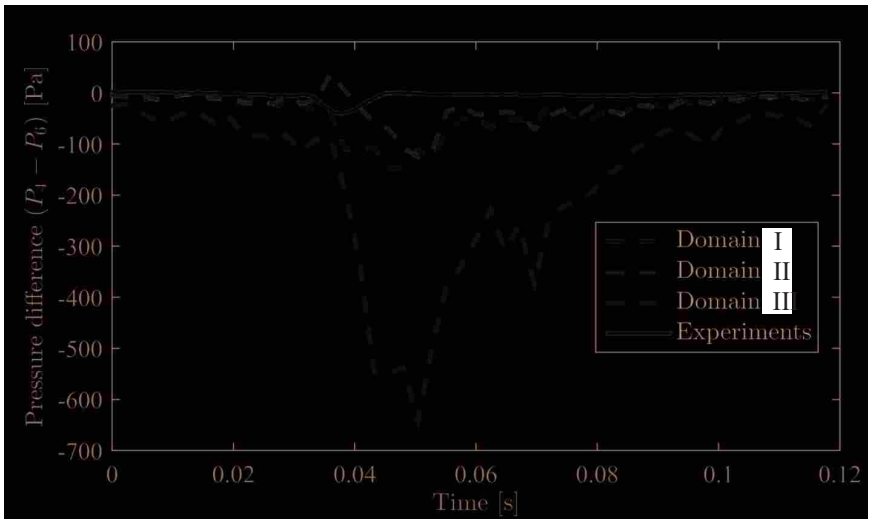

Figure 6.4: Comparison of pressure calculations in different domains (dashed lines) and experimental results (solid purple line).

$|| \epsilon_g ||_{L^2(\partial\Omega)}$ could be even larger than the error in the original experimental data. Remembering that the error level propagated to the pressure field is scaled by $A|| \epsilon_f ||_{L^2(\Omega)}$ when the area of the domain is large, it is expected to have large error for typically large error in data $|| \epsilon_f ||_{L^2(\Omega)}$ and domain area A. For example, for the pressure calculation in the domain I, the relative error comparing to the inlet kinematic pressure ($1/2\rho U_{max}^2 = 88.6\,\text{Pa}$) ranges from 0.5% to 170%. As a reference, the performance achieved by Charonko [3] gives around 33% to 75% error, but does not match the time history of the pressure transducer record. It is not fair to compare the result in this thesis to Charonko's [3] paper because of several differences including: domain sizes and shapes, post processing methods and governing equations. However, the large error yielded from both of these calculations implies that significant error propagation is inherent in the pressure Poison solver, rather than the details of the implementation.

It is also interesting that in Charonko's paper [3] comparing pressure calculation methods (Omni-direction integral and multi-path line integral method), the Poisson method gives largest error. This might be because the compatibility condition is not satisfied with pure Neumann boundary conditions, and the calculated error is intrinsically large with a relatively coarse mesh, and a low accuracy numerical scheme (a high accuracy numerical scheme might overwhelm the solver since the solution does not exist). Thus, we highly recommend applying Dirichlet boundary conditions on the domain if possible, unless the PIV results are very accurate. If pure Neumann boundaries

have to be employed, methods like the Omini-directional integral method [32] could be better candidates.

In future PIV-based pressure calculation research, It is recommended to use pressure transducers with point-wise validation (similar to the implementation in this chapter or in Charonko's paper [3]), especially when pure Neumann boundary conditions are used.

CHAPTER 7. OPEN PROBLEMS

In this section, two open problems rising from this dissertation study are introduced. These two problems can direct the future research efforts.

7.1 $|| \epsilon_u || \rightarrow || \epsilon_f ||$

The problem studied in chapter 4 refers to the error propagation from the *data* of the pressure Poisson equation ($f(\boldsymbol{u}), g(\boldsymbol{u})$, and $h(\boldsymbol{u})$) to the *solution*, which is the pressure field (p). With f as the representative of the data, this error propagation problem can be denoted as

$$|| \epsilon_f || \rightarrow || \epsilon_p ||. \tag{7.1}$$

Similarly, the manner in which the error in the velocity field propagates to the data can be denoted as

$$|| \epsilon_{\boldsymbol{u}} || \rightarrow || \epsilon_f ||. \tag{7.2}$$

Expression 7.1 and 7.2 together splice an entire problem: $|| \epsilon_{\boldsymbol{u}} || \rightarrow || \epsilon_f || \rightarrow || \epsilon_p ||$, so that the error propagation from the velocity field to the pressure field problem reads

$$|| \epsilon_{\boldsymbol{u}} || \rightarrow || \epsilon_p ||. \tag{7.3}$$

Chapter 4 has essentially provided a complete solution to the problem 7.1. In section 4.5, problem 7.2 is qualitatively analyzed, and it implies the reason why the profile of the flow matters when calculating a pressure field from PIV results. However, a quantitative error bound is still desired and an open problem is presented here:

Whether and how the data of the pressure Poisson equation $f(\boldsymbol{u})$ and $g(\boldsymbol{u})$ continuously depends on the velocity field $\boldsymbol{u}$, when equation 4.1 and 4.3 is satisfied, if L^2 or L^∞ norm can be used as a measure of the variables?

I tried to solve this problem with my committee, however, the problem may relate to the well-posedness of the Navier-Stokes equations and Euler equations, which is generally difficult due to the nonlinearity and unbounded property of the differential operators. A full solution to this problem is beyond my current knowledge and the scope of this research; I will give more effort to this problem in future work.

7.2 Worst case error problem

In this dissertation, we offer a preliminary explanation of the complexity of the PIV-based pressure calculation. The whole problem (error propagation of PIV-based pressure calculation) is like a Tangram puzzle whose seven pieces comprise a square (figure 7.1).

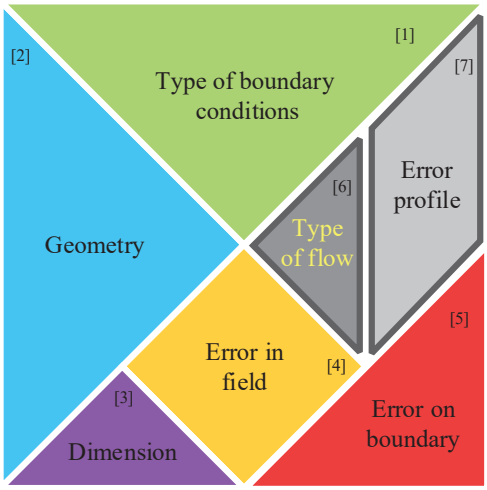

Figure 7.1: Overview of the whole ntire problem: solved (colored) and unsolved (gray) problems (pieces).

The colored pieces represent the pieces of the problem that are solved in chapter 4: why and how these factors (puzzle 1-5 : type of the boundary conditions, geometry of the domain, dimension of the domain, error level in the field and on the boundaries) dominate the error propagation dynamics in PIV-based pressure calculation. The two gray pieces represent problems that have

not been solved, in addition to the problem described in section 7.1 (how exactly the type of flow, or profile of the velocity field affects the error propagation). A simpler, yet important problem is understanding how the profile of the error in the velocity field affects the error level in the pressure field. A more specific statement of this problem is:

What type of error (or profile of error field) that has finite constant error level leads to the largest error in the pressure field? This type of error is called the "worst case error".

The opposite side of this problem is to figure out the "best case error", which consists of high error level in the velocity field but leads to relatively low error level in the pressure field after error propagation through the calculation. The solution to this problem can potentially guide experimental design: one should avoid the worst case error, and look for the best case error situations. A more important application is to design the synthetic flow field and corresponding worst case artificial error to test the performance of the PIV-based pressure calculation schemes.

I believe that the simplest of the two remaining problems is puzzle piece 7 (rather than 6), because it can be translated into a more tractable optimization problem (This is why the darker gray color is used for puzzle 6):

$$\begin{aligned} \max_{\epsilon_p} \quad & \frac{|| \epsilon_p ||^2_{L^2(\Omega)}}{||\nabla^2 \epsilon_p ||^2_{L^2(\Omega)}} \\ \text{sub.} \quad & \int_\Omega ||\nabla^2 \epsilon_p ||d\Omega = 1, \end{aligned} \tag{7.4}$$

which can be solved with optimal control or calculus of variations with some boundary conditions.

REFERENCES

[1] Van Oudheusden, B., 2013. "PIV-based pressure measurement." *Measurement Science and Technology,* **24**(3), p. 032001. 1, 2, 4, 20, 24

[2] Schwabe, M., 1935. "Über druckermittlung in der nichtstationären ebenen strömung." *Ingenieur-Archiv,* **6**(1), pp. 34–50. 2, 4

[3] Charonko, J. J., King, C. V., Smith, B. L., and Vlachos, P. P., 2010. "Assessment of pressure field calculations from particle image velocimetry measurements." *Measurement Science and Technology,* **21**(10), p. 105401. 2, 6, 7, 20, 21, 22, 23, 40, 53, 57, 58

[4] Dabiri, J. O., Bose, S., Gemmell, B. J., Colin, S. P., and Costello, J. H., 2013. "An algorithm to estimate unsteady and quasi-steady pressure fields from velocity field measurements." *The Journal of experimental biology*, pp. jeb–092767. 2, 5, 9, 21, 41

[5] King, C. V., and Smith, B. L., 2011. "Oscillating flow in a 2-d diffuser." *Experiments in fluids,* **51**(6), pp. 1577–1590. 2, 53

[6] Comte-Bellot, G., 1976. "Hot-wire anemometry." *Annual Review of Fluid Mechanics,* **8**(1), pp. 209–231. 3

[7] Ho, C.-M., and Tai, Y.-C., 1998. "Micro-electro-mechanical-systems (mems) and fluid flows." *Annual Review of Fluid Mechanics,* **30**(1), pp. 579–612. 3

[8] Durst, F., Melling, A., and Whitelaw, J. H., 1981. *Principles and practice of laser-Doppler anemometry*., Vol. 2 Academic press London. 3

[9] Willert, C. E., and Gharib, M., 1991. "Digital particle image velocimetry." *Experiments in fluids,* **10**(4), pp. 181–193. 3

[10] Adamczyk, A., and Rimai, L., 1988. "2-dimensional particle tracking velocimetry (PTV): technique and image processing algorithms." *Experiments in fluids,* **6**(6), pp. 373–380. 3

[11] Iungo, G. V., Viola, F., Camarri, S., Porté-Agel, F., and Gallaire, F., 2013. "Linear stability analysis of wind turbine wakes performed on wind tunnel measurements." *Journal of Fluid Mechanics,* **737**, pp. 499–526. 3

[12] Lou, W., Huang, M., Zhang, M., and Lin, N., 2012. "Experimental and zonal modeling for wind pressures on double-skin facades of a tall building." *Energy and Buildings,* **54**, pp. 179–191. 3

[13] Ran, B., and Katz, J., 1994. "Pressure fluctuations and their effect on cavitation inception within water jets." *Journal of Fluid Mechanics,* **262**, pp. 223–263. 3

[14] Gregory, J. W., Sakaue, H., Liu, T., and Sullivan, J. P., 2014. "Fast pressure-sensitive paint for flow and acoustic diagnostics." *Annual Review of Fluid Mechanics,* **46**, pp. 303–330. 3

[15] Fujii, S., Numata, D., Nagai, H., and Asai, K., 2013. "Development of ultrafast response anodized aluminum pressure-sensitive paints." In *51st AIAA Aerospace Sciences Meeting Including the New Horizons Forum and Aerospace Exposition, AIAA-2013-0485*. 3

[16] Kimura, F., McCann, J., Khalil, G. E., Dabiri, D., Xia, Y., and Callis, J. B., 2010. "Simultaneous velocity and pressure measurements using luminescent microspheres." *Review of Scientific Instruments,* **81**(6), p. 064101. 3

[17] Imaichi, K., and Ohmi, K., 1983. "Numerical processing of flow-visualization pictures–measurement of two-dimensional vortex flow." *Journal of Fluid Mechanics,* **129**, pp. 283–311. 4

[18] Adrian, R. J., 2005. "Twenty years of particle image velocimetry." *Experiments in fluids,* **39**(2), pp. 159–169. 4

[19] Elsinga, G. E., Scarano, F., Wieneke, B., and Van Oudheusden, B., 2006. "Tomographic particle image velocimetry." *Experiments in Fluids,* **41**(6), pp. 933–947. 4

[20] Belden, J., Truscott, T. T., Axiak, M. C., and Techet, A. H., 2010. "Three-dimensional synthetic aperture particle image velocimetry." *Measurement Science and Technology,* **21**(12), p. 125403. 4

[21] De Kat, R., and Van Oudheusden, B., 2012. "Instantaneous planar pressure determination from PIV in turbulent flow." *Experiments in fluids,* **52**(5), pp. 1089–1106. 4, 20, 24, 41, 52

[22] van Oudheusden, B. W., Scarano, F., Roosenboom, E. W., Casimiri, E. W., and Souverein, L. J., 2007. "Evaluation of integral forces and pressure fields from planar velocimetry data for incompressible and compressible flows." *Experiments in Fluids,* **43**(2-3), pp. 153–162. 5

[23] Van Oudheusden, B., 2008. "Principles and application of velocimetry-based planar pressure imaging in compressible flows with shocks." *Experiments in fluids,* **45**(4), pp. 657–674. 5

[24] Lignarolo, L., Ragni, D., Krishnaswami, C., Chen, Q., Ferreira, C. S., and Van Bussel, G., 2014. "Experimental analysis of the wake of a horizontal-axis wind-turbine model." *Renewable Energy,* **70**, pp. 31–46. 5, 36

[25] Villegas, A., and Diez, F. J., 2014. "On the quasi-instantaneous aerodynamic load and pressure field measurements on turbines by non-intrusive PIV." *Renewable Energy,* **63**, pp. 181–193. 5

[26] Panciroli, R., and Porfiri, M., 2013. "Evaluation of the pressure field on a rigid body entering a quiescent fluid through particle image velocimetry." *Experiments in fluids,* **54**(12), pp. 1–13. 5

[27] Nila, A., Vanlanduit, S., Vepa, S., and Van Paepegem, W., 2013. "A PIV-based method for estimating slamming loads during water entry of rigid bodies." *Measurement Science and Technology,* **24**(4), p. 045303. 5, 36

[28] Moore, P., Lorenzoni, V., and Scarano, F., 2011. "Two techniques for PIV-based aeroacoustic prediction and their application to a rod-airfoil experiment." *Experiments in fluids,* **50**(4), pp. 877–885. 5, 36

[29] Morris, S. C., 2011. "Shear-layer instabilities: particle image velocimetry measurements and implications for acoustics." *Annual Review of Fluid Mechanics,* **43**, pp. 529–550. 5

[30] Haigermoser, C., 2009. "Application of an acoustic analogy to PIV data from rectangular cavity flows." *Experiments in fluids,* **47**(1), pp. 145–157. 5

[31] Baur, T., and Köngeter, J., 1999. "PIV with high temporal resolution for the determination of local pressure reductions from coherent turbulence phenomena." In *International Workshop on PIV'99- Santa Barbara, 3rd, Santa Barbara, CA*, pp. 101–106. 5

[32] Liu, X., and Katz, J., 2006. "Instantaneous pressure and material acceleration measurements using a four-exposure PIV system." *Experiments in Fluids,* **41**(2), pp. 227–240. 5, 9, 21, 22, 24, 41, 58

[33] Azijli, I., Sciacchitano, A., Ragni, D., Palha da Silva Clerigo, A., and Dwight, R. P., 2015. "A posteriori uncertainty quantification of PIV-derived pressure fields." In *11th International Symposium on Particle Image Velocimetry, PIV15, Santa Barbara, CA, USA, September 14-16 2015; Authors version*. 6

[34] Oren, L., Khosla, S., and Gutmark, E., 2014. "Intraglottal geometry and velocity measurements in canine larynges." *The Journal of the Acoustical Society of America,* **135**(1), pp. 380–388. 7, 20

[35] Oren, L., Khosla, S., and Gutmark, E., 2014. "Intraglottal pressure distribution computed from empirical velocity data in canine larynx." *Journal of biomechanics,* **47**(6), pp. 1287–1293. 7, 20, 21, 36

[36] Maynes, R. D., 1997. "On rotating bluff-body flows.". 10

[37] Smith, S. L., and Thomson, S. L., 2013. "Influence of subglottic stenosis on the flow-induced vibration of a computational vocal fold model." *Journal of fluids and structures,* **38**, pp. 77–91. 13

[38] Shurtz, T. E., and Thomson, S. L., 2013. "Influence of numerical model decisions on the flow-induced vibration of a computational vocal fold model." *Computers & structures,* **122**, pp. 44–54. 13

[39] Daily, D. J., and Thomson, S. L., 2013. "Acoustically-coupled flow-induced vibration of a computational vocal fold model." *Computers & structures,* **116**, pp. 50–58. 13

[40] Kähler, C. J., Scharnowski, S., and Cierpka, C., 2012. "On the uncertainty of digital PIV and ptv near walls." *Experiments in fluids,* **52**(6), pp. 1641–1656. 16

[41] Foucaut, J.-M., and Stanislas, M., 2002. "Some considerations on the accuracy and frequency response of some derivative filters applied to particle image velocimetry vector fields." *Measurement Science and Technology,* **13**(7), p. 1058. 20

[42] Reimer, A. S., and Cheviakov, A. F., 2013. "A matlab-based finite-difference solver for the poisson problem with mixed dirichlet–neumann boundary conditions." *Computer Physics Communications,* **184**(3), pp. 783–798. 28

[43] Neeteson, N. J., Bhattacharya, S., Rival, D. E., Michaelis, D., Schanz, D., and Schröder, A., 2015. "Pressure-field extraction from lagrangian flow measurements." In *11th International Symposium on Particle Image Velocimetry, PIV15, Santa Barbara, CA, USA, September 14-16 2015*. 35, 36

[44] Löhrer, B., Valiorgue, P., Ben Hadid, H., Fröhlich, J., and Doppler, D., 2015. "Pressure measurements using particle image velocimetry in the vicinity of a flexible moving structure." In *11th International Symposium on Particle Image Velocimetry, PIV15, Santa Barbara, CA, USA, September 14-16 2015; Authors version*. 35, 36

[45] Villegas, A., and Diez, F., 2014. "Evaluation of unsteady pressure fields and forces in rotating airfoils from time-resolved PIV." *Experiments in Fluids,* **55**(4), pp. 1–17. 35, 36

[46] Jalalisendi, M., Panciroli, R., Cha, Y., and Porfiri, M., 2014. "A particle image velocimetry study of the flow physics generated by a thin lamina oscillating in a viscous fluid." *Journal of Applied Physics,* **115**(5), p. 054901. 36

[47] de Kat, R., and Ganapathisubramani, B., 2013. "Pressure from particle image velocimetry for convective flows: a taylor's hypothesis approach." *Measurement Science and Technology,* **24**(2), p. 024002. 36

[48] Novara, M., and Scarano, F., 2013. "A particle-tracking approach for accurate material derivative measurements with tomographic PIV." *Experiments in fluids,* **54**(8), pp. 1–12. 36

[49] Pröbsting, S., Scarano, F., Bernardini, M., and Pirozzoli, S., 2013. "On the estimation of wall pressure coherence using time-resolved tomographic PIV." *Experiments in fluids,* **54**(7), pp. 1–15. 36

[50] Albrecht, T., del Campo, V., Weier, T., Metzkes, H., and Stiller, J., 2013. "Deriving forces from 2d velocity field measurements." *The European Physical Journal Special Topics,* **220**(1), pp. 91–100. 36

[51] Ghaemi, S., and Scarano, F., 2013. "Turbulent structure of high-amplitude pressure peaks within the turbulent boundary layer." *Journal of Fluid Mechanics,* **735**, pp. 381–426. 36

[52] Ghaemi, S., Ragni, D., and Scarano, F., 2012. "PIV-based pressure fluctuations in the turbulent boundary layer." *Experiments in fluids,* **53**(6), pp. 1823–1840. 36

[53] Koschatzky, V., Westerweel, J., and Boersma, B., 2011. "A study on the application of two different acoustic analogies to experimental PIV data." *Physics of Fluids (1994-present),* **23**(6), p. 065112. 36

[54] Violato, D., Moore, P., and Scarano, F., 2011. "Lagrangian and eulerian pressure field evaluation of rod-airfoil flow from time-resolved tomographic PIV." *Experiments in fluids,* **50**(4), pp. 1057–1070. 36

[55] Brachet, M. E., Meiron, D. I., Orszag, S. A., Nickel, B., Morf, R. H., and Frisch, U., 1983. "Small-scale structure of the Taylor–Green vortex." *Journal of Fluid Mechanics,* **130**, pp. 411–452. 43

[56] Smith, B., and Swift, G., 2001. "Measuring second-order time-average pressure." *The Journal of the Acoustical Society of America,* **110**(2), pp. 717–723. 53

[57] Smith, B. L., and Swift, G., 2003. "Power dissipation and time-averaged pressure in oscillating flow through a sudden area change." *The Journal of the Acoustical Society of America,* **113**(5), pp. 2455–2463. 53

[58] Foias, C., Manley, O., Rosa, R., and Temam, R., 2001. *Navier-Stokes equations and turbulence*., Vol. 83 Cambridge University Press. 69

[59] Gould, S. H., 1995. *Variational methods for eigenvalue problems: an introduction to the methods of Rayleigh, Ritz, Weinstein, and Aronszajn*. Courier Corporation. 73

APPENDIX A. DERIVATION OF ERROR BOUNDS

A.1 Inequalities and notation

We only require three inequalities for the results obtained here, i.e. for bounds on the L^2 norm of the error. Similar calculations can be performed to obtain bounds on the L^∞ norm of the error, but the analysis is far more complicated and hence is omitted. We also point out that these inequalities are valid only when both sides are finite, i.e. the relevant functions live in the appropriate function spaces. For further details on such inequalities, we refer to standard textbooks such as [58].

1. Cauchy-Schwarz:
$$\left| \int_\Omega f(x)g(x)dS \right| \leq |\Omega| \|f\|_{L^2(\Omega)} \|g\|_{L^2(\Omega)}. \tag{A.1}$$

2. Poincare:
$$\|f\|_{L^2(\Omega)} \leq C \|\nabla f\|_{L^2(\Omega)}, \tag{A.2}$$
where C is the Poincare constant that depends both on the boundary conditions and the geometry of the domain. C can also be thought of as the square of the reciprocal of the smallest eigenvalue of the Laplace operator acting on the domain Ω with the same boundary conditions as those prescribed to f.

3. Minkowski (triangle inequality):
$$\|f+g\|_{L^2(\Omega)} \leq \|f\|_{L^2(\Omega)} + \|g\|_{L^2(\Omega)}. \tag{A.3}$$

A.2 Error bounds in L^2 space

A.2.1 Dirichlet case

Using the principle of superposition and the linearity of the Poisson pressure equation, we can rewrite the solution to equation (4.7) and (4.8) as $\epsilon_p = \epsilon_{p(\mathscr{L})} + \epsilon_{p(\mathscr{P})}$, where

$$\begin{aligned} \nabla^2 \epsilon_{p(\mathscr{L})} &= 0 \quad in \quad \Omega \\ \epsilon_{p(\mathscr{L})} &= \epsilon_h \quad on \quad \partial\Omega, \end{aligned} \tag{A.4}$$

and

$$\begin{aligned} \nabla^2 \epsilon_{p(\mathscr{P})} &= \epsilon_f \quad in \quad \Omega \\ \epsilon_{p(\mathscr{P})} &= 0 \quad on \quad \partial\Omega. \end{aligned} \tag{A.5}$$

Equation (A.4), which is harmonic, satisfies the maximum principle:

$$|| \epsilon_{p(\mathscr{L})} ||_{L^2(\Omega)} \leq \sqrt{\frac{\int_\Omega \| \epsilon_h \|^2_{L^\infty(\partial\Omega)} dS}{|\Omega|}} = || \epsilon_h ||_{L^\infty(\partial\Omega)}, \tag{A.6}$$

where $|\Omega|$ refers to the area or volume of the region Ω.

Now multiplying (A.5) by $\epsilon_{p(\mathscr{P})}$ and integrating over the entire domain, we have

$$\int_\Omega \epsilon_{p(\mathscr{P})} \nabla^2 \epsilon_{p(\mathscr{P})} \, \mathrm{d}S = \int_\Omega \epsilon_{p(\mathscr{P})} \epsilon_f \, \mathrm{d}S. \tag{A.7}$$

Integrating by parts equation A.7 yields

$$\oint_{\partial\Omega} \epsilon_{p(\mathscr{P})} \nabla \epsilon_{p(\mathscr{P})} \cdot \mathbf{n} \mathrm{d}L - \int_\Omega \nabla \epsilon^2_{p(\mathscr{P})} \, \mathrm{d}S = \int_\Omega \epsilon_{p(\mathscr{P})} \epsilon_f \, \mathrm{d}S. \tag{A.8}$$

Substituting homogeneous BCs to equation (A.8), we have

$$\int_\Omega \nabla \epsilon^2_{p(\mathscr{P})} \, \mathrm{d}S = -\int_\Omega \epsilon_{p(\mathscr{P})} \epsilon_f \, \mathrm{d}S. \tag{A.9}$$

This can be rewritten as

$$\|\nabla\, \epsilon_{p(\mathscr{P})}\, \|^2_{L^2(\Omega)} = -\frac{1}{|\Omega|}\int_\Omega \epsilon_{p(\mathscr{P})}\epsilon_f \, \mathrm{d}S. \tag{A.10}$$

Applying Poincare and Cauchy–Schwarz inequalities (A.10) yields

$$||\, \epsilon_{p(\mathscr{P})}\, ||^2_{L^2(\Omega)} \leq C_D||\, \epsilon_{p(\mathscr{P})}\, ||_{L^2(\Omega)}||\, \epsilon_f\, ||_{L^2(\Omega)}, \tag{A.11}$$

where, C_D is the Poincare constant for the Dirichlet boundary value problem.

Combining (A.6) and (A.11), and using the Minkowski inequality we have

$$||\epsilon_p||_{L^2(\Omega)} = ||\epsilon_{p(\mathscr{P})} + \epsilon_{p(\mathscr{L})}||_{L^2(\Omega)} \leq C_D||\epsilon_f||_{L^2(\Omega)} + ||\epsilon_h||_{L^\infty(\partial\Omega)}. \tag{A.12}$$

A.2.2 Neumann BCs

Similar to the Dirichlet case, the Poisson equation with nonhomogeneous Neumann BCs 4.7 and 4.9 can be solved by superimposing a Poisson equation with homogeneous BCs

$$\begin{aligned} &\nabla^2\, \epsilon_{p(\mathscr{P})} = \epsilon_f \quad in \quad \Omega \\ &\nabla\, \epsilon_{p(\mathscr{P})} \cdot \mathbf{n} = 0 \quad on \quad \partial\Omega, \end{aligned} \tag{A.13}$$

and a Laplace equation with nonhomogeneous BCs

$$\begin{aligned} &\nabla^2\, \epsilon_{p(\mathscr{L})} = 0 \quad in \quad \Omega \\ &\nabla\, \epsilon_{p(\mathscr{L})} = \epsilon_g \quad on \quad \partial\Omega. \end{aligned} \tag{A.14}$$

Solutions of (A.13) exist only when the compatibility condition

$$\int_\Omega \epsilon_f \, dS = 0 \tag{A.15}$$

is satisfied, which means the mean value of the error in the data is assumed zero. With this in mind, we multiply A.13 with $\epsilon_{p(\mathscr{P})}$ and integrate over the entire domain, integrating by parts and using

the homogeneous boundary conditions to arrive at:

$$||\nabla\, \epsilon_{p(\mathscr{P})}\, ||^2_{L^2(\Omega)} = |\Omega|^{-1} \int_\Omega |\nabla\, \epsilon_{p(\mathscr{P})}\, |^2 \mathrm{d}S = -|\Omega|^{-1} \int_\Omega \epsilon_{p(\mathscr{P})} \epsilon_f \, \mathrm{d}S. \tag{A.16}$$

Applying the Cauchy–Schwarz and Poincare inequalities, we see that

$$\frac{1}{C_N} ||\epsilon_{p(\mathscr{P})} - \bar{\epsilon}_{p(\mathscr{P})}||^2_{L^2(\Omega)} \leq ||\nabla\, \epsilon_{p(\mathscr{P})}||^2_{L^2(\Omega)} \leq ||\epsilon_{p(\mathscr{P})}||_{L^2(\Omega)} ||\epsilon_f||_{L^2(\Omega)}, \tag{A.17}$$

where C_N is the Poincare constant for these boundary conditions and $\bar{\epsilon}_{p(\mathscr{P})} = \int_\Omega \epsilon_{p(\mathscr{P})}\, \mathrm{d}S$, the mean of the pressure field. The compatibility condition on the boundary condition allows us to assume that $\bar{\epsilon}_{p(\mathscr{P})}$ vanishes, and thus $||\epsilon_{p(\mathscr{P})}||_{L^2(\Omega)}$ can be bounded as

$$||\, \epsilon_{p(\mathscr{P})}\, ||_{L^2(\Omega)} \leq C_N ||\epsilon_f||_{L^2(\Omega)}. \tag{A.18}$$

A similar approach to (A.14) yields

$$\|\nabla\, \epsilon_{p(\mathscr{L})}\|^2_{L^2(\Omega)} = |\Omega|^{-1} \int_\Omega |\nabla\, \epsilon_{p(\mathscr{L})}\, |^2 \mathrm{d}S = |\Omega|^{-1} \oint_{\partial\Omega} \epsilon_{p(\mathscr{L})} \epsilon_g \, \mathrm{d}L. \tag{A.19}$$

Using the Poincare inequality twice on the domain and boundary, respectively,

$$\begin{aligned} \frac{1}{C_N} ||\epsilon_{p(\mathscr{L})} - \bar{\epsilon}_{p(\mathscr{L})}||^2_{L^2(\Omega)} \leq ||\nabla\, \epsilon_{p(\mathscr{L})}||^2_{L^2(\Omega)} &\leq \frac{|\partial\Omega|}{|\Omega|} ||\epsilon_{p(\mathscr{L})}||_{L^2(\partial\Omega)} ||\epsilon_g||_{L^2(\partial\Omega)} \\ &\leq C_{NB} \frac{|\partial\Omega|}{|\Omega|} ||\nabla\, \epsilon_{p(\mathscr{L})}||_{L^2(\partial\Omega)} ||\epsilon_g||_{L^2(\partial\Omega)} \\ &= C_{NB} \frac{|\partial\Omega|}{|\Omega|} ||\epsilon_g||^2_{L^2(\partial\Omega)}. \end{aligned} \tag{A.20}$$

Assuming $||\bar{\epsilon}_{p(\mathscr{L})}||_{L^2(\Omega)}$ vanishes, and combining (A.18) and (A.20) we have

$$||\epsilon_p||_{L^2(\Omega)} = ||\, \epsilon_{p(\mathscr{P})} + \epsilon_{p(\mathscr{L})}\, ||_{L^2(\Omega)} \leq C_N ||\epsilon_f||_{L^2(\Omega)} + \sqrt{C_N C_{NB}} ||\epsilon_g||_{L^2(\partial\Omega)} \sqrt{\frac{|\partial\Omega|}{|\Omega|}}, \tag{A.21}$$

where, C_{NB} is the Poincare constant for the specified boundary conditions. We note that the constant on the boundary is due to the compatibility condition, i.e. the error on the boundary is mean zero.

A.3 Calculation of the Poincare constants

For a smooth and bounded domain, the optimal (minimum) Poincare constant for the Laplace operators is the reciprocal of the first eigenvalue of the BVP problem. As examples, we list the exact Poincare constant for the simple cases illustrated in the paper. For the pure Dirichlet BC case in $M \times N$ domain, the first eigenvalue is $\lambda_1 = \pi^2/M^2 + \pi^2/N^2$, and thus the Poincare constant is $C_D = \lambda_1^{-1} = \pi^2(MN)^2/(M^2+N^2)$. Similarly, for the pure Neumann boundary case, the optimal Poincare constant is $C_N = \max\left(M^2/\pi^2, N^2/\pi^2\right)$, and for the boundary, $C_{NB} = 2(M+N)/\pi$. The exact optimal Poincare constant calculation is generally difficult for an arbitrary domain, however, Rayleigh quotient and Rayleigh quotient iteration can be employed to numerically estimate the optimal Poincare constant. See [59] for one approach to estimating the eigenvalues of such operators.